Issue 2-4

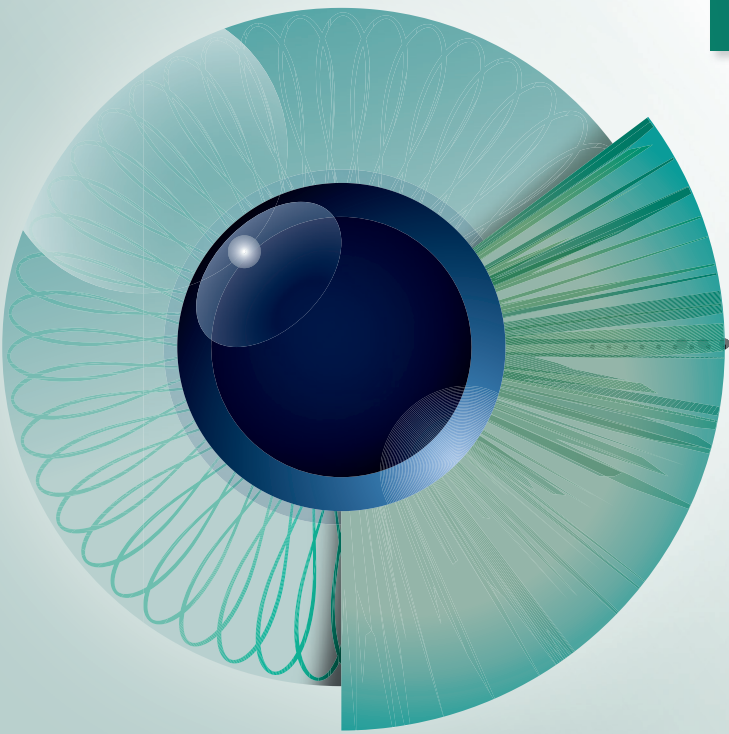

Journal for Modeling in Ophthalmology

JMO
Journal for Modeling in Ophthalmology

Journal for Modeling in Ophthalmology (JMO) was created in 2014 with the aim of providing a forum for interdisciplinary approaches integrating mathematical and computational modeling techniques to address open problems in ophthalmology.

The Editorial Board members include experts in ophthalmology, physiology, mathematics, and engineering, and strive to ensure the highest scientific level of the contributions selected for publication. JMO aims to be the voice for this rapidly growing interdisciplinary research and we hope you will join us on this exciting journey.

JMO welcomes articles that use modeling techniques to investigate questions related to the anatomy, physiology, and function of the eye in health and disease.

For further information on JMO's focus and scope as well as manuscript submissions:

www.modeling-ophthalmology.com
info@modeling-ophthalmology.com

Copyright

Publisher
Kugler Publications
P.O. Box 20538
1001 NM Amsterdam
The Netherlands
info@kuglerpublications.com
www.kuglerpublications.com

ISSN
Online: 2468-3930
Print: 2468-3922

Manuscript submissions
Author guidelines and templates are available via the website, through which all manuscripts should be submitted. For inquiries please contact us via e-mail.

Publication frequency
JMO is published four issues per year (quarterly) electronically. A selection is published in print twice a year and distributed free of charge at congresses through Kugler Publications or partners.

Advertising inquiries
JMO offers online and in print sponsorship and advertising opportunities. Please contact Kugler Publications to for inquiries.

b. After 12 months from the date of publication, authors are able to enter into separate, additional contractual arrangements for the non-exclusive distribution of JMO's published version of the work, with an acknowledgement of its initial publication in JMO.

Open access policy

The first volume of JMO is fully open access (after registration) without requiring any publication fee from the authors. However, we are currently evaluating various models to cover the publications costs while keeping knowledge as accessible as possible, which remains our first priority. Possible models include subscription fees, publication fees, and advertisement venues, or a combination. Please share your thoughts with us on this hot topic via e-mail.

Disclaimers

Table of contents

Editorial

Original articles

© Journal for Modeling in Ophthalmology 2020;4:4-10
Editorial

Modeling the eye as a window on the body

Lucia Carichino[1], Simone Cassani[2], Sergey Lapin[3], Alice Verticchio Vercellin[4-6]

[1]School of Mathematical Sciences, Rochester Institute of Technology, Rochester, NY, USA; [2]Department of Mathematics, University at Buffalo, SUNY, Buffalo, NY, USA; [3]Department of Mathematics and Statistics, Washington State University, Pullman, Washington, USA; [4]University of Pavia, Pavia, Italy; [5]IRCCS – Fondazione Bietti, Rome, Italy; [6]Department of Ophthalmology, Icahn School of Medicine at Mount Sinai Hospital, New York, NY, USA

Keywords: mathematical modeling, multidisciplinary approach, ocular and systemic diseases

1. Introduction

Systemic pathologies such as diabetes and arterial hypertension affect different organs and systems in the body.[1-4] However, the first signs of these pathologies often emerge as functional and structural alterations in the eye.[1-4] As a consequence, the ophthalmologist is often the first physician to make a diagnosis of systemic diseases. In fact, the eye represents a unique organ where signs of systemic diseases may be assessed with noninvasive techniques.[3] The vessels of the retinal microcirculation are the only ones in the whole body where the physician, via the examination of the *fundus oculi*, can observe vessel health directly and noninvasively. In this sense, the diagnosis and follow-up of important systemic conditions, such as diabetes and arterial hypertension, is performed by the periodical examination of the *fundus oculi*. The assessment of visual acuity is a tool for early diagnosis of diabetes since high glucose levels in the aqueous humor, the fluid filling the anterior and posterior chamber of the eye, are correlated to a myopic shift in the visual acuity. The visual field examination allows to assess both ophthalmological diseases, such as glaucoma, and neurological ones, such as brain tumors, cerebral ischemia, or multiples sclerosis, of which the most common first manifestation is a retrobulbar optic neuritis[3]. If not promptly diagnosed and treated, the complications of the aforementioned diseases – such as cardiovascular disorders, nephropathy, and neuropathies – are potentially

Correspondence: Lucia Carichino, Rochester Institute of Technology, School of Mathematical Sciences, 85 Lomb Memorial Drive, Rochester, NY 14623, USA.
E-mail: lcsma1@rit.edu

harmful for the health of the individual. Therefore, the eye examination is important to make an early diagnosis of such diseases and to prevent clinical complications.

Mathematical modeling represents an important tool that can help in the analysis, early diagnosis, and treatment of systemic and ocular diseases.[5-8] In order to build mathematical models that can work in synergy with clinical data, it is important to create active interdisciplinary collaborations between experts in different mathematical areas and medical professionals. The workshop "Modeling the eye as a window on the body" that was held in San Jose, CA, USA October 15-19 2018, brought together experts in mathematical modeling of the eye and other organs in the body, medical doctors, statisticians, and biomedical engineers to share their perspectives and expertise with the final goal to develop mathematical models linking the eye to the body.

Mathematical models represent a virtual lab that can be used to:

1. elucidate the driving mechanisms leading to a pathology;
2. isolate and quantify the relative contribution of factors that cannot be separated *in vivo*; and
3. test clinical hypotheses.

To date, only preliminary mathematical models linking ocular dynamics with the cardiovascular system and the dynamics in other organs, such as the kidney and brain, are available.[9] Several mathematical models studying systems separately have been previously developed;[6-8] however, the coupling of the different vascular and structural components involved introduces multiple challenges. Specifically, the coupling involves the following multiscale and multiphysics components: fluid flows (*e.g.* aqueous humor, blood, and urine), structural deformations, oxygen transport, pressurized ambients, local vascular regulatory mechanisms, and micro- and macro-vasculature networks. This will require sophisticated mathematical techniques such as systems of mixed hyperbolic, parabolic, and elliptic partial differential equations involving multiple time scales. Therefore, this project endeavors active collaborations among experts in different mathematical areas, such as differential equations, fluid structure interaction, reduced and compartmental models, and numerical analysis. Since the condition of the eye is indicative of the one of other organs, it is important to define coupled mathematical models that can correlate and/or predict the effect of different diseases in different anatomical regions.

Statistical analysis and clinical data are essential to consolidate model predictions. In medicine, statistical analysis is one of the most common uses of mathematics to extrapolate significant correlations in the data. Moreover, statistical analysis, mathematical models, and clinical data can be used in synergy to build reliable and accurate models by parameter estimation, to validate model results with data, and to elucidate the mechanisms behind clinical correlations.[10-13] The Structured Quartet Research Ensemble (SQuaRE) on "Ocular blood flow and its role in development of glaucoma", held at The American Institute of Mathematics (AIM) in 2017, is an example of how an integrative collaboration between mathematics, ophthalmology, and statistics can

provide better medical care for patients with various complicated diseases, such as glaucoma. The results of this collaborative effort have been published in scientific and clinical journals.[11-12]

2. Workshop "Modeling the eye as a window on the body"

The workshop "Modeling the eye as a window on the body" brought together twenty participants among leading experts and new researchers (young faculty members, postdoctoral, and graduate students) from universities in the United States, Canada, Great Britain, Italy and France, with the following common goals:

1. Provide a forum to discuss how to address the challenges of the mathematical coupling of the eye to the rest of the body.
2. Exchange ideas on the potential of using mathematical models of the eye to:
   - Get insights on the effects of aging and systemic pathologies, such as arterial hypertension and diabetes, on the ocular structure and functionality.
   - Achieve a better understanding of the processes that regulate the level of intraocular pressure (IOP) and oxygenation in the retinal tissue.
3. Identify the clinical questions of interest for the coupled mathematical models under investigation.

To achieve these goals, the participants attended lectures in the morning and participated in group activities in the afternoon focused on specific topics. Of note, the groups were organized in such a way that each one contained at least one expert in medicine.

3. Workshop lectures

The workshop lectures aimed to discuss the current state of the art and open problems from various points of view: clinical, mathematical, statistical, and engineering. Among the notable lectures given by the workshop participants, we list a number of them below.

From the clinical perspective, Carlo Bruttini (University of Pavia, Pavia, Italy) presented a review of the relationship between the eye and vascular systemic pathologies, with a special focus on diabetic retinopathy,[1,3] thrombosis and occlusions of ocular vessels,[3] and the effect of high altitude on the production and drainage of aqueous humor,[14] which regulates IOP.

From the mathematical perspective, Giovanna Guidoboni (University of Missouri, Columbia, MO, USA) discussed the state of the art of modeling in ophthalmology, focusing on mathematical models developed to study ocular hemodynamics, ocular structural deformation, aqueous humor production, and retinal oxygenation.[5]

The mathematical models presented have been used in synergy with clinical data to interpret medical measurements, and to try to isolate the different pathogenic mechanisms that could lead to the specific results observed in each individual patient. Anita Layton (University of Waterloo, Waterloo, Canada) presented multiscale mathematical models of kidney physiology and pathophysiology to study the role of the kidney in regulating blood flow and blood pressure.[15] In particular, the presentation focused on the role played by mathematical models in the understanding of the mechanisms underlying any potential cardiovascular benefit of kidney-targeting drugs for diabetes.[16]

From the engineering perspective, Giovanni Ometto (City, University of London, London, United Kingdom) presented recent work on image processing of retinal fundus photographs. The image-processing algorithm developed was used to detect positions of microaneurisms in diabetic patients. The algorithm, in synergy with statistical analysis, was employed to identify the area where lesions could predict progression to vision-threatening diabetic retinopathy.[17]

From the statistical perspective, Yuan Wang (Washington State University, Pullman, WA, USA) presented results on statistical analysis techniques to study tree-structured data, focusing on applications related to the brain artery tree.[18] Andrea Arnold (Worcester Polytechnic Institute, Worcester, MA, USA) presented a review of the Bayesian approach for state and parameter estimation using nonlinear Kalman filtering and data.[19]

4. Future research directions

As a result of the workshop lectures and group discussions, the participants identified the following topics of interest for future research. Each topic includes challenges from the mathematical perspective while addressing questions of significant clinical relevance.

4.1. Aqueous humor physiology and IOP

Aqueous humor, the fluid filling the anterior and posterior chamber of the eye, has many important functions, among which is the regulation of IOP.[3] Aqueous humor production involves a filtration process from the fenestrated capillaries of the ciliary body. This process is similar to the kidney nephron glomerular filtration.[22] Hence, the idea is to develop a compartmental model of aqueous humor production inspired by existing kidney models that could account for the effects of IOP-lowering medications with several mechanisms of action on the different ion channels. The preliminary results of this collaboration were presented as poster at the 2019 Association for Research in Vision and Ophthalmology (ARVO) Annual Meeting in Vancouver, Canada.[23]

4.2. Neovascularization in wet age-related macular degeneration (AMD)

AMD neovascularization is responsible for severe vision loss,[3] and modeling this phenomenon involves sophisticated multiphase and multiscale modeling techniques. Only a few mathematical models of AMD choroidal neovascularization are available in the literature.[20-21] The participants discussed the importance of developing a model that includes the effect of anti-vascular endothelial growth factor (anti-VEGF) treatments on the neovascularization growth. The model will then be used in synergy with clinical images of choroidal neovascularization, acquired with optical coherence tomography (OCT) and OCT angiography, to investigate the mechanisms behind the differences in anti-VEGF treatment efficiency in individual patients.

4.3. Age and retrobulbar blood flow

Color Doppler imaging (CDI) is a common imaging technique used to assess the blood flow velocities in several vessels in the body. Specifically in the eye, blood flow velocities are assessed in the retrobulbar vessels (ophthalmic artery, central retinal artery, and posterior ciliary arteries) and the participants shared their knowledge about the hemodynamic changes in glaucoma.[24] In the future, the use of CDI to assess and compare blood flow in the retrobulbar circulation and in other parts of the body in both elderly and young subjects can further the understanding of the role of aging in the pathophysiology of ocular and systemic diseases.

4.4. Oxygenation in light and darkness

It has been reported in the clinical literature that retinal oxygen saturation is higher in dark than light in healthy humans.[25] This result is conjectured to be the effect of different changes in the metabolic consumption of the tissue in the inner and outer retina in dark and light. To explore this hypothesis, the participants utilized a coupled model of the retinal vasculature and retinal tissue oxygen saturation.[26] The model was used to obtain preliminary results relative to the effect of changes in the metabolic consumption of the different retinal tissue layers on the level of retinal oxygen saturation. The model will be further improved and used to determine the underlying mechanisms governing oxygen saturation and tissue consumption in the retinal tissue to achieve a better understanding of the results recorded in the clinical literature.

4.5. Imaging predictors of diabetes progression

A number of imaging techniques, such as fluorescein angiography and OCT,[1] are currently used to evaluate retinal lesions due to diabetic retinopathy. The aforementioned imaging tools are used for early diagnosis of diabetic retinopathy, and to detect and predict the disease progression. The participants discussed the potential use of CDI and CDI-derived parameters previously used for glaucoma (*i.e.* velocity waveform parameters in the ophthalmic artery, central retinal artery, and posterior

ciliary arteries), for the assessment and early detection of disease progression in patients with diabetic retinopathy.

5. Conclusions

A fruitful collaboration between mathematicians and medical professionals can significantly contribute to both better mathematical descriptions of human physiology and improved medical procedures. In this context, the workshop “Modeling the eye as a window on the body” led to the creation of an international network of experts in different fields that will continue to collaborate to further the development of medical and mathematical research, and to pursue multiple directions for future research in different fields. The insights coming from this interdisciplinary collaboration may ultimately aid the future development of new techniques and instruments designed by biomedical engineers for the diagnosis and treatment of systemic and ophthalmological pathologies.

Acknowledgements

The authors would like to thank the American Institute of Mathematics (AIM) staff and all the participants of the workshop “Modeling the eye as a window on the body” for their help and support.

The authors have no financial or proprietary interest in any material or method mentioned. The contribution of the author Dr. Alice C. Verticchio Vercellin was supported by Fondazione Roma and by the Italian Ministry of Health.

References

1. Shotliff K, Duncan G. Diabetes and the eye. In: KM Shaw, MH Cummings, editors. Diabetes: Chronic Complications. Chichester: John Wiley and Sons; 2005.
2. Konstantinidis L, Guex-Crosier Y. Hypertension and the eye. Curr Opin Ophthalmol. 2016;27(6):514-521.
3. Kansky JJ. Clinical ophthalmology: A systemic approach. 8th edition. Elsevier; 2015.
4. Flammer J, Konieczka K, Bruno R, Virdis A, Flammer AJ, Taddei S. The eye and the heart. Eur Heart J. 2013;34(17):1270-1278.
5. Gross JC, Harris A, Siesky BA, Sacco R, Shah A, Guidoboni G. Mathematical modeling for novel treatment approaches to open-angle glaucoma. Exp Rev Ophthalmol. 2017;(12)6:443-455.
6. Guidoboni G., Harris A., Sacco R. Ocular Fluid Dynamics. Anatomy, Physiology, Imaging Techniques, and Mathematical Modeling. New York: Springer-Birkhauser; 2019.
7. Ottesen JT, Danielsen M, editors. Mathematical modelling in medicine. Amsterdam: IOS Press; 2000.

8. Layton AT, Edwards A. Mathematical Modeling in Renal Physiology. Springer; 2014.
9. Salerni F, Repetto R, Harris A, Pinsky P, Prud'homme C, Szopos M, Guidoboni G. Biofluid modeling of the coupled eye-brain system and insights into simulated microgravity conditions. PLoS One. 2019;14;14(8):e0216012.
10. Carichino L, Harris A, Guidoboni G, et al. A theoretical investigation of the increase in venous oxygen saturation levels in glaucoma patients. Journal for Modeling in Ophthalmology. 2016;1(1):64-87.
11. Carichino L, Guidoboni G, Verticchio Vercellin AC. Computer-aided identification of novel ophthalmic artery waveform parameters in healthy subjects and glaucoma patients. Journal for Modeling in Ophthalmology 2016;1(2):59-69.
12. Carichino L, Harris A, Lapin S. Waveform parameters of retrobulbar vessels in glaucoma patients with different demograpics and disease severity. Eur J Ophthalmol. 2019;7:1120672119848259.
13. Marquis AD, Arnold A, Dean-Bernhoft C, Carlson BE, Olufsen MS. Practical identifiability and uncertainty quantification of a pulsatile cardiovascular model. Math Biosci. 2018;304:9-24.
14. Bruttini C, Verticchio Vercellin AC, Montanaro B. The Mont Blanc Study - The effect of altitude on intraocular pressure and central corneal thickness in healthy volunteers. Invest Ophthalmol Vis Sci. 2018;59(9):1662. Abstract 1662. ARVO, April 29-May 3, 2018, Honolulu, HI.
15. Leete J, Layton AT. Sex-specific long-term blood pressure regulation: Modeling and analysis. Comput Biol Med. 2019;104:139-148.
16. Layton, AT. Optimizing SGLT inhibitor treatment for diabetes with chronic kidney diseases. Biol Cybern. 2019;113(1-2):139-148.
17. Ometto G, Assheton P, Calivá F, et al. Spatial distribution of early red lesions is a risk factor for development of vision-threatening diabetic retinopathy. Diabetologia. 2017;60(12):2361-2367.
18. Wang Y, Marron JS, Aydin LA, Bullitt E, Wang HA. Nonparametric regression model with tree- structured response. J Am Stat Assoc. 2012;107:1272-1285.
19. Arnold A, Calvetti D, Somersalo E. Parameter estimation for stiff deterministic dynamical systems via ensemble Kalman filter. Inverse Probl. 2014:30(10): 105008.
20. Shirinifard A, Glazier JA, Swat M,. Adhesion failures determine the pattern of choroidal neovascularization in the eye: a computer simulation study. PLoS Computat Biol. 2012;8(5):e1002440.
21. Zhu S, Shi F, Xiang D, Zhu W, Chen H, Chen X. Choroid neovascularization growth prediction with treatment based on reaction-diffusion model in 3-d oct images. IEEE J Biomed Health Inform. 2017;21(6):1667-1674.
22. Koeppen BM., Stanton BA. Berne and Levy Physiology. 7th edition. Elsevier; 2017.
23. Guidoboni G, Bonifazi, G, Sacco R, et al. Electrochemical characterization of ciliary epithelium physiology: a theoretical approach. Invest Ophthalmol Vis Sci. 2019; 60(9):3202. Abstract 3202. ARVO, April 28- May 2, 2019. Vancouver, Canada.
24. Stalmans I, Vandewalle E, Anderson DR, et al. Use of colour Doppler imaging in ocular blood flow research. Acta Ophthalmol. 2011;89(8):e609-30. doi:10.1111/j.1755-3768.2011.02178.x.
25. Hardarson SH, Basit S, Jonsdottir TE, et al. Oxygen saturation in human retinal vessels is higher in dark than in light. Invest Ophthalmol Vis Sci. 2009;50:2308-2311. doi:10.1167/iovs.08-2576.
26. Cassani S. Blood circulation and aqueous humor flow in the eye: multi-scale modeling and clinical applications. Ph.D. thesis, Purdue University 2016.

© Journal for Modeling in Ophthalmology 2020;4:11-33
Original article

On the recovery of the stress-free configuration of the human cornea

Andrea Montanino[1], Anna Pandolfi[2]

[1]*Dipartimento di Strutture per l'Ingegneria e l'Architettura, Università degli Studi di Napoli "Federico II", Napoli, Italy*, [2]*Dipartimento di Ingegneria Civile ed Ambientale, Politecnico di Milano, Milano, Italy*

Abstract

Purpose: The geometries used to conduct numerical simulations of the biomechanics of the human cornea are reconstructed from images of the physiological configuration of the system, which is not in a stress-free state because of the interaction with the surrounding tissues. If the goal of the simulation is a realistic estimation of the mechanical engagement of the system, it is mandatory to obtain a stress-free configuration to which the external actions can be applied.
Methods: Starting from a unique physiological image, the search of the stress-free configuration must be based on methods of inverse analysis. Inverse analysis assumes the knowledge of one or more geometrical configurations and, chosen a material model, obtains the optimal values of the material parameters that provide the numerical configurations closest to the physiological images. Given the multiplicity of available material models, the solution is not unique.
Results: Three exemplary material models are used in this study to demonstrate that the obtained, non-unique, stress-free configuration is indeed strongly dependent on both material model and on material parameters.
Conclusion: The likeliness of recovering the actual stress-free configuration of the human cornea can be improved by using and comparing two or more imaged configurations of the same cornea.

Keywords: human cornea, inverse analysis, parameter identification, postoperative cornea, preoperative cornea, stress-free configuration

Correspondence: Dipartimento di Ingegneria Civile ed Ambientale, Politecnico di Milano, P.za Leonardo da Vinci, 32 - 20133 Milano, Italy.
E-mail: anna.pandolfi@polimi.it

1. Introduction

Among all the soft biological tissues of the human body, the cornea is unique because of the transparency[1] and the accessibility of its location. These features make the cornea one of the most deeply studied and better known biological materials, since advanced optical imaging has revealed all the details of the underlying microstructure.[2,3]

The cornea belongs to the system of lenses that in the eye deviate the light rays onto the specialized receptor cells of the retina. When the lens system is defective, the image appears blurred and unfocused, requiring the use of additional lenses to perceive a correct image. Spectacles and contact lenses have been and are largely used, but in the last two decades laser technology has allowed to correct refraction errors permanently by modifying the refractive power of cornea, in consideration of the accessibility of the organ. The change of the corneal refractive power is principally obtained by selective laser ablation of some portions of the tissue,[4] or by the insertion of small prosthesis or devices (arcuates, intraocular lenses, rings, etc.) within the cornea. Refractive surgery technologies have become very safe and precise, but still gross errors are occurring occasionally when the cornea presents geometrical or structural anomalies. For non-standard corneas that must undergo refractive surgery, the support of a numerical model of the cornea with patient-specific features may become of great importance to reduce the possibility of mistakes and to help in the selection and design of the optimal treatment.

A numerical model of the human cornea must be constructed accounting for all the important features of the tissue. Given the refractive function of the cornea, the adoption of the patient-specific shape is a must. Nowadays, the availability of optical apparatuses makes trivial the attainment of the customized shape that can be transferred in the solid model of the cornea.[5]

As a soft biological tissue, the cornea is very deformable and water rich, and therefore, almost incompressible. The mechanical behavior in physiological conditions is characterized by reversibility even at large deformations. Relaxation experiments on pig corneas have revealed a viscous-plastic-damaging behavior.[6] Nevertheless, in applications concerning refractive surgery, degenerative aspects should not be of relevance, since the postoperative cornea is supposed to behave in a reversible way as in the preoperative conditions. Thus, in the literature it has become customary to adopt finite strain hyperelastic models for the material, which imply directly reversibility.[7,8]

Although the corneal tissue is organized in five layers, from the mechanical point of view the most important properties are related to collagen, the structural component of the stroma, the central and thicker layer. Stromal collagen, immersed in a matrix of elastin and proteoglycans, is organized hierarchically in fibrils and lamellae following a complex architecture that has been observed more than three decades ago.[2] In the central area of the cornea the lamellae are preferentially oriented in two directions: nasal-temporal (NI) and superior-inferior (SI). This organization involves approximately 60% of the fibrils, while the remaining 40% are randomly oriented.

The change in curvature in the limbus zone is related to the presence of a consistent amount of fibrils aligned in the circumferential direction.[9] The distribution of the fibrils is not homogeneous across the corneal thickness. Biomedical imaging has revealed recently that collagen lamellae in the posterior cornea are commonly twice as thick as those in the anterior[10] and interlamellar interaction results from interweaving,[11] leading to a shear stiffness three times larger than the one in the posterior third of the stroma.[12] At the limbus, the larger stiffness is shown at the posterior side, where the limbus merges with the iris.[13] The architecture of the cornea confers obvious characteristics of inhomogeneity and anisotropy to the material. Thus, the material response varies with the position on the mid-surface, with the position across the thickness of the cornea, and with the direction of loading, and these features are very important in establishing the optimal state under physiological conditions. The optimal state must be intended from the energetic point of view, as a configuration characterized by a minimum of the mechanical energy of the system, where the stresses are balancing the external actions. In particular, the cornea is stressed by the intraocular pressure (IOP) exerted by the aqueous humor that fills the anterior chamber of the eye.

The configuration of the cornea taken by optical imaging (physiological configuration) is stressed, and as such, the geometrical models of the cornea obtained by imaging cannot be directly used in numerical applications. Models require to be integrated by accounting for the unknown physiological stress state in the imaged configuration (pre-stress approach;[7]) or by detecting a stress free geometrical configuration to which the IOP is applied.[8,14] In fact, if the imaged geometry is used directly, the application of the IOP on the posterior surface of the cornea will modify ostensibly the configuration of the cornea, changing the refractive power and the stress state. As in other biological cases, a correct modeling of the cornea requires to recover the stress-free configuration (also known as natural configuration) to which the external actions are applied. The configuration reached by the system under the proper actions will coincide, in this way, to the physiological configuration. The procedure used to recover the stress-free state of a system can be named identification of the natural configuration.

The importance of the recovery of the stress-free geometry in human arteries has been pointed out in Raghavan et al.,[15] where an iterative procedure based on the observation of the self-similarity of the shape of abdominal aortic aneurisms under different blood pressures was used. More recently, a backward displacement method able to solve the inverse problem iteratively using fixed point iterations was described by Bols et al.[16,17] The correct estimate of the physiological stress state is an important task for arterial walls, loaded by the blood pressure. Disregarding or approximating in a rough way the physiological stress invalidates the predictions on aneurysm formations and vessel ruptures.[18–20] The importance of the prestress in scleral shells has been pointed out also by Grytz and Downs,[14] who developed a Forward Incremental Prestressing Method for the computation of the prestress in the physiological configuration.

As far as the cornea is concerned, the need to recover the stress-free state has been considered in several contributions. An approach based on iterative estimation of the physiological stress was proposed in Pinsky et al.[7] A method based on the modification of the coordinates of the discretized model has been proposed in Pandolfi and Manganiello,[8] and the same concept has been applied in subsequent works.[21–23] A similar procedure has been used by Ariza-Gracia's group.[24–27] A variational approach based on iterative finite element solutions was proposed in a study by Otani and Tanaka.[28]

The approaches described in the literature have a comparable validity, as long as they are able to reconstruct the physiological state in terms of stresses and strains. What has not been sufficiently emphasized is that the stress-free configuration is dependent on the chosen material model and on the values of the material parameters. Identification procedures have been used in combination with Mooney-Rivlin material models,[29] Ogden material models,[30] neo-Hookean material models,[31] Yeoh material models,[27] or with more realistic fiber reinforced models.[8,22,23,32] Clearly, the predicted stress state in physiological conditions will be very different in all these cases.

The dependence on material model and parameters renders the identification of the stress-free geometry very delicate and not definitive. The consequence of this uncertainty is that, for a chosen material model, the identification of the stress-free geometry cannot be disjointed from the simultaneous identification of the material parameters. This means that a single configuration, or a single image, is not sufficient to characterize at once geometry and materials, calling for the need of conducting *in-vivo* tests on each patient.[26,33] Furthermore, no useful information of the *in-vivo* mechanical properties can be derived from *ex-vivo* tests,[34] which deal with a completely different material removed from its natural environment. Possible candidates for the use in identification procedures are the probe test[35] and the air puff test.[25,26,36–39]

As an alterative, when two images corresponding to two different configurations of the same cornea are available, it is possible to characterize a reduced selection of the material parameters together with the stress-free configuration. This can be possible, for example, when images of the same cornea in preoperative and postoperative conditions are available. The approach has been used in a rather successful way in several works using anisotropic material models with inclusion of the fibril microstructure and considering preoperative and postoperative geometries of corneas that underwent photo-refractive keratectomy (PRK),[5,32,36,37,40] but an accurate analysis on the influence of the material model on the identified material properties and stress-free geometry has never been conducted.

Goal of this study is to gain awareness on the relevance on the choice of a material model in the identification of the stress-free configuration and of the material parameters.

Therefore, we consider a set of patient-specific corneas that underwent laser reprofiling surgery (PRK) and three material models characterized by a growing complexity: the isotropic Hooke material model extended to the finite kinematics, the Mooney-Rivlin material model, and the sophisticated anisotropic model proposed in

Pandolfi and Vasta.[23] We describe the approach for the simultaneous identification of the natural configuration and a limited number of material properties of the adopted material models, present the results obtained on the set of patient specific corneas, and discuss the numerical findings in view of possible applications.

2. Methods

The procedure of the identification of the stress-free geometry and of a selected number of material parameters based on the comparison of the preoperative and postoperative physiological configurations of a PRK-ablated cornea has been conceived on the following idea.[40]

Cornea reprofiling conducted with laser ablation removes the anterior tissues of the cornea, including epithelium, Bowman's membrane and a certain amount of the anterior stromal tissue. Clearly, ablation burns the tissue, and causes temporary modifications in the immediately adjacent tissues that need a week or more to heal and renew the epithelial layer. Since the posterior surface of the cornea is not directly touched by the laser, it is possible to make the assumption that the posterior third of the cornea is not affected. An additional assumption is that IOP is not modified by refractive surgery.

The stress-free configuration is intended as an ideal non-physiological state where the material is not loaded, or the IOP is zero. The stress-free state is not known, and cannot be achieved under *in vivo* conditions, but it can be estimated through an inverse numerical calculation. Having chosen a material model and a set of material parameters, a numerical analysis where the posterior surface of the cornea is pressurized with the physiological IOP will provide, as solution, the displacement field associated to the stresses that balance the IOP by means of the material model. The displacements modify the cornal configuration, which will not longer respect the physiological shape.

Let us now assume to subtract the computed displacements to the original coordinates of the cornea in the physiological configuration. The resulting configuration will be less convex than the physiological configuration. If a new analysis under the same IOP is conducted on the modified geometry, the resulting stressed geometry will be closer to the physiological geometry. Clearly, there will be differences related to the fact that the analysis has to be conducted in finite kinematics, which induces geometrical non-linearity; therefore the procedure must be repeated several times using an iterative algorithm that will be interrupted when the desired precision is reached.

The same procedure can be applied to the preoperative and postoperative configurations of the corneas, using the same material model and parameters. If the choice of material model and parameters are correct, the posterior surfaces of the stress-free geometries of the two cases will coincide. If they do not, the material model, the material parameters, or both are not correct.

The discrepancy between the coordinates of the posterior surfaces of the preop-

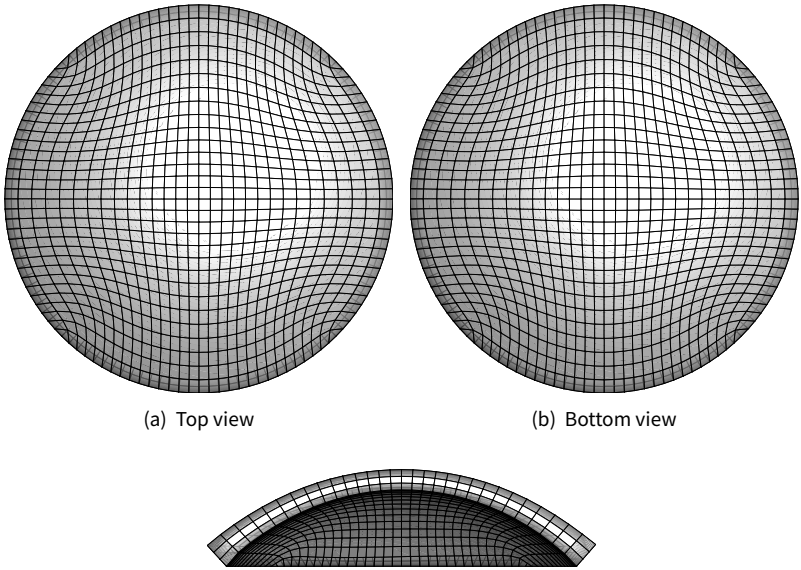

(a) Top view (b) Bottom view

(c) Section

Fig. 1. Example of finite element discretization for one of the corneas considered in this study. The geometry refers to the physiological preoperative configuration.

erative and postoperative stress-free geometries can be taken as a measure of the likeness (ML) of the material parameters for the adopted material model. The ML can then be used to identify the optimal set of material parameters for the patient-specific cornea.

The actual procedure is described in detail in the following section.

2.1 Recovery of the stress-free configuration of the cornea

Twelve pairs of preoperative and postoperative corneal geometries were chosen in a random way from a large set of informed patients that underwent PRK refractive surgery. The data used in this work were collected by the same experienced surgeon using a high definition corneal tomographer coupled with a pachymeter, according to a protocol approved by the Italian Data Protection Authority and to the principles expressed in the Declaration of Helsinki. Purely geometrical data elaborated from the images by the tomographer were anonymized and de-identified prior to the transmission to us and disjoined from all the other clinical information (age, gender, ethnicity, and IOP).

Data are provided as a list of coordinate of a cloud of points representing the anterior and posterior surface of the cornea in preoperative or postoperative configu-

ration. The data are elaborated through a software to produce a solid model of the cornea discretized in finite elements, as shown in Figure 1.

To each cornea, we apply the procedure proposed firstly in Pandolfi and Manganiello.[8] The algorithm of identification of the stress-free geometry begins with the construction of the mesh in the physiological configuration, seen as a final target of the iterative process. Each step consists in the application on the posterior surface of the cornea of the patient-specific IOP, keeping the limbus constrained to rotate in order to maintain the cross-section always orthogonal to the deformed mid-surface of the cornea. The rotating boundaries have been proved to be the ones that optimize the refractive behavior of the cornea in the physiological IOP range.[21] The solution of the static problem with an assigned material model provides the set of displacements employed in the iterative algorithm to compute the stress-free configuration. The iterative process ends when, within an assigned tolerance ϵ, the deformed configuration superposes the target physiological configuration. The algorithm is described in Algorithm. 1

Algorithm 1 Unstressed geometry recovery algorithm, as proposed in Pandolfi and Manganiello[8]

Set $\mathbf{X}_0$ as the nodal coordinates corresponding to the physiological IOP.
Set $k = 1$
Set $\mathbf{X}^k = \mathbf{X}_0$
for $k \leq k_{\max}$ **do**
  Assign the physiological IOP on the posterior surface of the cornea
  Solve the static problem and obtain the k-th nodal displacements $\mathbf{u}^k$
  Compute the k-th physiological nodal coordinates $\mathbf{x}^k = \mathbf{X}^k + \mathbf{u}^k$
  Compute the coordinate difference $\Delta\mathbf{X} = \mathbf{X}_0 - \mathbf{x}^k$ and the corresponding norm $|\Delta\mathbf{X}|$
  if $|\Delta\mathbf{X}| < \epsilon|\mathbf{X}^0|$ **then**
    Exit
  end if
  Set $\mathbf{X}^{k+1} = \mathbf{X}_0 - \mathbf{u}^k$
  Set $k = k + 1$
end for

2.2 Identification of the optimal material properties

For the chosen material model, the identification of the optimal material properties is achieved by comparing the coordinates of the nodes lying on the posterior surface of the same cornea in the preoperative and postoperative configurations. In the following, the set of p material properties is referred to as $\mathbf{c} = \{c_2, c_2, \ldots, c_p\}$. Note that, in general, the material property set will include material parameters, parameters related to inhomogeneity and anisotropy distribution, variability across the thickness,

and others. Moreover, the set might not include all the parameters of the chosen material model; when a parameter is sufficiently well characterized by other means, it might be excluded from the $\mathbf{c}$ set.

The recovery procedure described in the previous section is applied to both the preoperative and postoperative configuration, using the same material properties and the same IOP, leading to two sets of nodal coordinates, $\mathbf{X}^{\mathrm{pre}}$ and $\mathbf{X}^{\mathrm{post}}$, respectively. Both sets will be dependent on the material properties.

Given the obvious difference in the geometry due to the cornea reprofiling, the comparison between stress-free preoperative and postoperative configuration can be conducted only on the nodes lying on the posterior surface of the cornea. The coordinates of the nodes of the posterior surface are collected in the subsets $\mathbf{Y}^{\mathrm{pre}}$ and $\mathbf{Y}^{\mathrm{post}}$, respectively.

We introduce the index ML representing a *measure of likeness* of the property set $\mathbf{c}$ as

$$\mathrm{ML}(\mathbf{c}) = \frac{|\mathbf{Y}^{\mathrm{post}} - \mathbf{Y}^{\mathrm{pre}}|}{|\mathbf{Y}^{\mathrm{pre}}|} \tag{1}$$

where the norm $|\mathbf{X}|$ is defined as

$$|\mathbf{X}| = \sqrt{\sum_{1}^{N} (X_1^2 + X_2^2 + X_3^2)} \tag{2}$$

and N is the number of elements in the subsets $\mathbf{X}$. Clearly, the more likely the material properties are, the smaller is the value of the ML index. Thus, the identification procedure can be stated as an optimization problem

$$\mathbf{c}^{\mathrm{opt}} = \arg\min_{\mathbf{c}} \mathrm{ML}(\mathbf{c})\,. \tag{3}$$

In this work, the search for the optimal values of the parameters is organized by spanning discrete values of the p parameters within a realistic range, determined through a few preliminary calculations. For each set of values of p, we apply the iterative recovery procedure for both preoperative and postoperative cases and compute the ML index. Since each evaluation of ML involves a certain number of finite element analyses, the efficiency of the approach is clearly related to the chosen material model, which may affect considerably the computational time requested by the static solution.

In the following calculations, the missing value of the patient-specific IOP is assumed to be equal to 14 mmHg (1.87 kPa) for all cases.

3. Results

The method is applied to three different material models. The first material model is a Hooke material extended to the finite kinematics. The second material model

is a Mooney-Rivlin model. The third material model is the second order approximation anisotropic model, accounting for the complex architecture of distributed collagen fibrils within the cornea, described in Pandolfi and Vasta[23] and used in previously cited studies.[5,32].

3.1 Hooke material model extended to finite kinematics

The material model considered here is a fictitious material, since it adopts the Hooke model to finite kinematic stress and strain measure. The model can be expressed through the strain energy density

$$\Psi_{\mathrm{Hooke}} = \frac{1}{2}\mathbf{E} : \mathbb{D}(E,\nu)\mathbf{E}\,, \qquad \mathbf{S} = \frac{\partial \Psi_{\mathrm{Hooke}}}{\partial \mathbf{E}} \tag{4}$$

where $\mathbf{E}$ is the Green-Lagrange strain tensor, $\mathbf{S}$ the second Piola-Kirchhoff tensor, and $\mathbb{D}$ is the isotropic constant constitutive tensor, dependent on the Young's modulus E and on the Poisson's coefficient ν. We assume that Poisson's coefficient is known, and set it to $\nu = 0.45$, thus the parameter drops from the set $\mathbf{c}$. The optimization problem in Eq. (3) reduces to

$$E^{\mathrm{opt}} = \arg\min_{E} \mathrm{ML}(E)\,. \tag{5}$$

Table 1. Geometrical characteristics of the baseline cornea.

Geometrical parameter	mm
Average anterior surface in-plane radius (AAR)	5.8100
Average posterior surface in-plane radius (APR)	5.2900
Pre-operative central corneal thickness (BCCT)	0.5117
Post-operative central corneal thickness (ACCT)	0.4414
Maximum ablation profile depth (ΔCCT)	0.0720

The approach is described in detail with reference to one of the patient-specific corneas (heretofore referred to as baseline analysis), characterized by the geometrical parameters listed in Table 1. We begin by constructing a finite element mesh from the supplied tomographer data. The mesh, shown in Figure 1, consists of 2,700 exahedron solid elements, with 30 elements along the NT and SI meridians, and 3 elements across the thickness.

Figure 2 compares the physiological preoperative and postoperative configurations of the NT meridional section of the baseline cornea, as obtained from the tomographer images, showing the whole section Fig. 2(a), and a detail of the optical zone at the center, Fig. 2(b). Images visualize clearly the reshaping induced by the PRK reprofiling and, moreover, testify the forward deflection of the posterior surface induced by the reduction in corneal stiffness.

The optimal value of Young's modulus is obtained by running several recovery analyses with the preoperative and postoperative geometries, assuming for E the discrete values 0.25, 0.375, 0.5, 0.625, 0.75, 1, and 1.25 MPa. The dependence of the ML

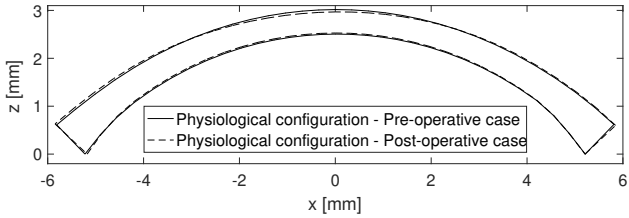

(a) Whole

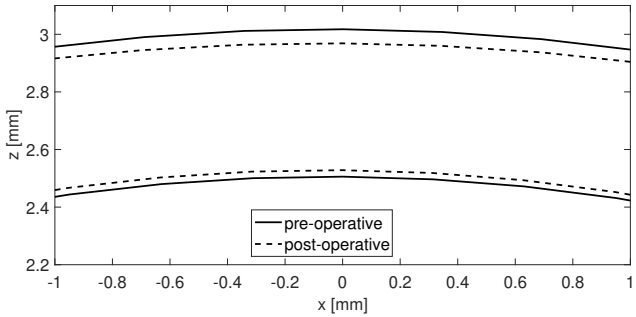

(b) Central Detail

Fig. 2. Baseline cornea, Hooke material. Physiological preoperative and postoperative configurations of the cornea across the NT meridian, as provided by the tomographer. (*a*) Whole extension. (*b*) Detail in the central optical zone.

index on E is shown in Figure 3. The minimum value of the ML index, corresponding to 2.546×10^{-5} is located at $E^{\mathrm{opt}} = 0.625$ MPa. Figure 4 compares the recovered stress-free preoperative and postoperative geometries corresponding to the optimal value E^{opt}, showing the good correspondence of the position of the posterior surfaces.

The role played by Young's modulus on the recovered stress-free geometry is shown with the aid of Figure 5. Starting from the same physiological postoperative configuration and assuming two different values for Young's modulus, 0.25 MPa and 1.25 MPa, respectively, the recovered geometries are ostensibly different.

The analysis described for the baseline cornea was repeated for 12 pairs of corneal geometries, whose geometrical parameters are listed in Table 2. The baseline cornea is labelled 1S. The same table also lists the minimum value of the $\mathrm{ML}^{\mathrm{opt}}$ index and the corresponding E^{opt}.

Table 2. Geometrical characteristics of the 12 human corneas used in this study. AAR: average anterior radius

Cornea	AAR mm	APR mm	BCCT mm	ACCT mm	ΔCCT mm	E^{opt} MPa	ML^{opt}
1S	5.812	5.29	0.512	0.440	0.072	0.625	2.546 10^{-5}
1D	5.820	5.19	0.506	0.449	0.057	0.750	3.304 10^{-6}
2S	5.570	5.00	0.540	0.425	0.115	0.750	3.415 10^{-5}
2D	5.529	4.96	0.535	0.403	0.132	1.000	1.672 10^{-5}
3S	5.579	5.00	0.501	0.462	0.039	0.500	3.180 10^{-5}
3D	5.529	5.02	0.509	0.471	0.038	0.500	2.116 10^{-5}
4S	5.525	5.01	0.567	0.502	0.065	< 0.125	–
4D	5.538	5.03	0.564	0.473	0.091	0.125	3.020 10^{-4}
5S	5.786	5.29	0.523	0.458	0.065	< 0.125	–
5D	5.873	5.32	0.530	0.452	0.078	–	–
6S	5.507	4.98	0.597	0.436	0.161	< 0.125	–
6D	5.590	5.04	0.553	0.438	0.115	< 0.125	–
Average	5.622	5.076	0.539	0.452	0.087	0.413	–
Std dev	0.134	0.131	0.028	0.024	0.036	0.308	–

APR: average posterior radius. BCCT: Preoperative central corneal thickness. ACCT: post-operative central corneal thickness. ΔCCT: central ablation depth. E^{opt}: optimal value of the Young's modulus. ML^{opt}: minimum value of the ML

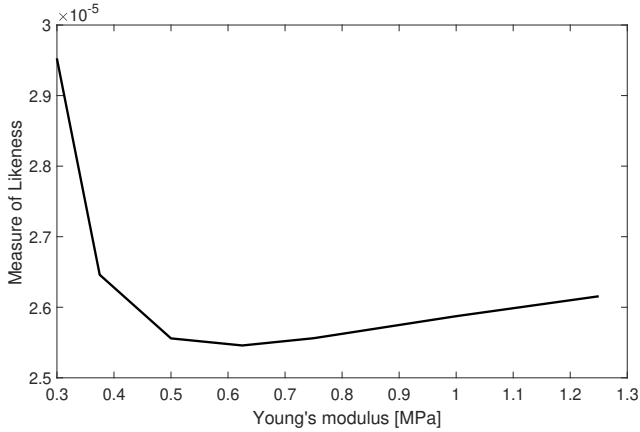

Fig. 3. Baseline cornea with Hooke material model. Dependence of the ML index on the Young's modulus.

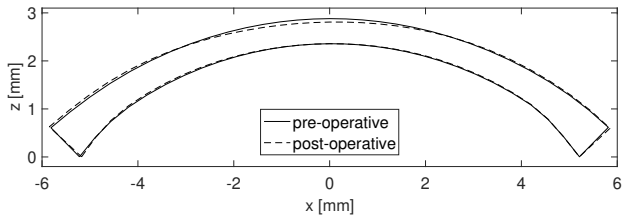

Fig. 4. Baseline cornea with Hooke material model. Comparison between the recovered stress-free preoperative and postoperative geometries for the optimal value of Young's modulus, $E^{\mathrm{opt}} = 0.625$ MPa.

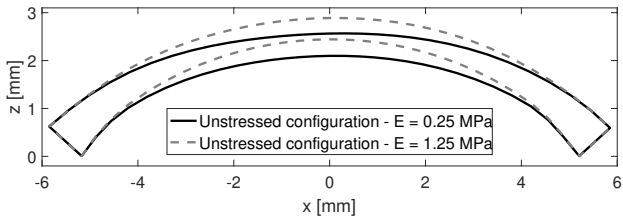

Fig. 5. Baseline cornea with Hooke material model. Comparison between the recovered stress-free preoperative geometries obtained with two different values of Young's modulus E, *i. e.*, 0.25 MPa and 1.25 MPa, respectively.

Table 2 shows that, within the explored range $E = \{0.25, 1.25\}$ MPa, the corneas labelled 1S, 1D, 2S, 2D, 3S, and 3D are characterized by a minimum value of the ML index, and the corresponding E^{opt} falls in the range $\{0.5, 1\}$ MPa. Regrettably a minimum was not detected for the corneas labelled 4S, 4D, 5D, 5S, 6D, and 6S. Corneas labelled 4S, 4D, 5S, 6S, and 6D reveal an increasing trend, and the minimum ML index might fall below $E = 0.25$ MPa. The cornea labelled 5D, instead, shows a decreasing trend that may be ascribed to an imprecise detection of the postoperative image that does not allow alignment to the preoperative image.

To investigate the behavior of the corneas that failed to show a minimum in the range $E = \{0.25, 1.25\}$ MPa, for the sole cornea 4D the analysis has been extended to a wider range exploring the values E = 0.2, 0.1125, 0.12, 0.125, 0.13, 0.1375, and 0.15 MPa. The second search revealed a minimum of the ML index for E = 0.125 MPa (Fig. 6). Interestingly, the ML^{opt} is one order or magnitude larger than in the cases

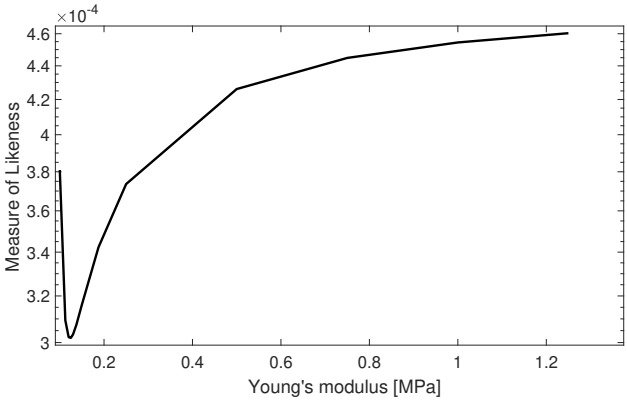

Fig. 6. Anomalous cornea 4D with Hooke material model. Dependence of the ML index on Young's modulus.

that provided a good response in the reduced range of E, suggesting that some discrepancy characterizes the data obtained from the preoperative and postoperative images. The discrepancy is indeed confirmed by the comparison of the recovered stress-free preoperative and postoperative geometries, that, for the optimal values of the Young's modulus E^{opt} = 0.125 MPa does not show any agreement on the shape of the posterior surface (Fig. 7).

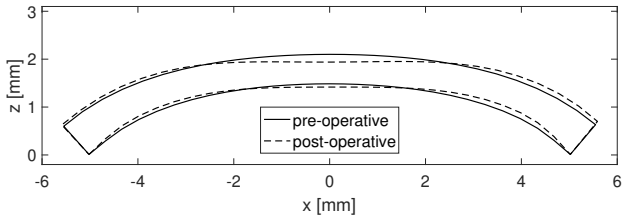

Fig. 7. Anomalous cornea 4D with Hooke material model. Comparison of the recovered stressed-free preoperative and postoperative geometries, at the optimal Young's modulus $E^{\mathrm{opt}} = 0.125$ MPa.

3.2 Mooney-Rivlin material model

The quasi-incompressible version of the isotropic Mooney-Rivlin material model is governed by a strain energy function of the form

$$\Psi_{\mathrm{MR}} = \frac{1}{4}K(J^2 - 1 - 2\log J) + \frac{1}{2}\mu_1(\bar{I}_1 - 3) + \frac{1}{2}\mu_2(\bar{I}_2 - 3) \tag{6}$$

where J is the determinant of the deformation tensor $\mathbf{F}$, $\bar{I}_1$ and $\bar{I}_2$ are the first and second invariant of the isochoric part of the Cauchy-Green strain tensor $\bar{\mathbf{C}} = J^{-2/3}\mathbf{F}^T\mathbf{F}$, K is a stiffness-like coefficient used to enforce the incompressibility of the material, and μ_1, μ_2 are shear stiffness parameters related to the shear modulus of the material as $\mu = \mu_1 + \mu_2$.

In order to reduce the number of parameters to identify to μ_1 and μ_2, given the meaning of a penalization coefficient for K, we set $K = 7$ MPa in all the calculations.

As already mentioned, in the present work we did not use a true optimization algorithm to detect the optimal values of the parameters, but performed multiple iterative recovery procedures over discrete sets of values. To reduce the heaviness of the calculations in the case of the two-parameter Mooney-Rivlin model, the search for the optimal pair of parameters has been restricted in a rather arbitrary way by performing a two-phase search. In the first phase, we constrain the two parameters to assume the same value and search the optimal value of $\mu_2 = \mu_1$ over discrete values within a wide range. In the second phase, we constrain μ_1 to the fixed optimal value and perform a second search on μ_2 again over a discrete set of values (Fig. 8). Clearly, since the two searches are discrete and constrained, the algorithm reduces in a sensible way the possibility to find the absolute minimum; thus the present results have to be considered only in a demonstrative way. In particular, we remark that the two parameters cannot be identified in a unique way, since we are comparing only two configurations.

We replicate for the baseline cornea 1D the optimization search conducted for the case of a Hooke material model. The optimization of the parameter μ_1 (solid line in

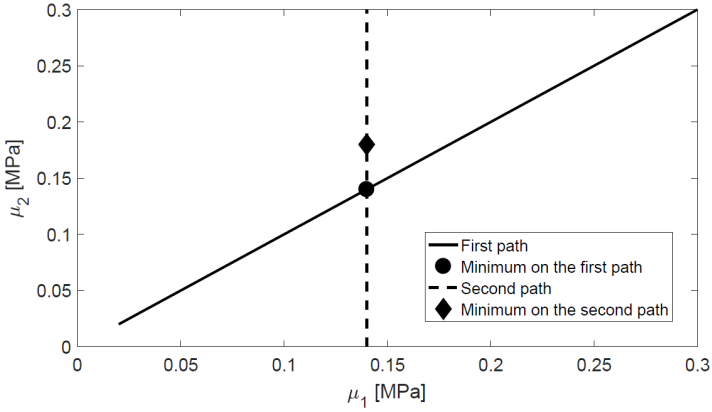

Fig. 8. Visualization of the search strategy adopted for the shear stiffness parameters μ_1 and μ_2 of the Mooney-Rivlin material model.

Fig. 8) gives $\mu_1^{\text{opt}} = \mu_2 = 0.14$ MPa. The dependence of the ML index on μ_1 can be observed in Figure 9(a).

Next, the parameter $\mu_1^{\text{opt}} = 0.14$ MPa is kept fixed at the optimal value, and the ML index is computed for μ_2 in the range $\{-0.06, 0.30\}$ MPa (dashed line in Fig. 8). The dependence of the ML index on μ_2 is shown in Figure 9(b). The optimal value of $\mu_2^{\text{opt}} = 0.18$ MPa is obtained for a value of ML = 7.453 $\times 10^{-6}$ one order of magnitude inferior to the best value obtained for the Hooke material model.

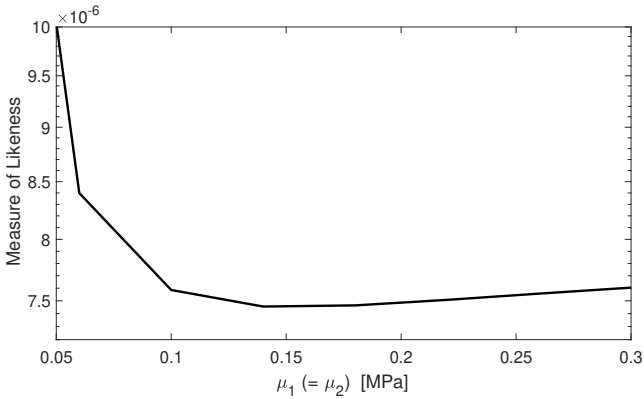

(a) First search

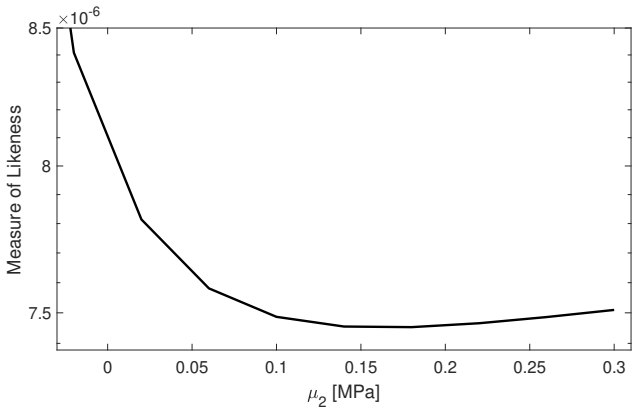

(b) Second search

Fig. 9. Baseline cornea with Mooney-Rivlin material. (*a*) Dependence of the ML index on the first shear stiffness parameter μ_1, under the constraint $\mu_2 = \mu_1$. (*b*) Dependence of the ML index on the second shear stiffness parameter μ_2 for a fixed value $\mu_1 = 0.14$ MPa.

3.3 Anisotropic distributed fiber reinforced material model

The anisotropic distributed fiber reinforced material model here considered is an advanced second order model that accounts for the average and the variance of two distributions of fibers. The model has been developed in Pandolfi and Vasta[23] and applied successfully to the modelling of the human cornea in several applications.[5,32,40] The model can be thought as an extension of the Mooney-Rivlin material model to account for the anisotropy induced by the presence of dispersed reinforcing fibers

embedded into an isotropic matrix. The strain energy function has the form

$$\Psi_{\mathrm{V}} = \Psi_{MR} + \sum_{M=1}^{2} \frac{k_{1M}}{2k_{2\,M}} \exp\left[k_{2\,M}(\bar{I}^{*}_{4\,M} - 1)^{2}\right]\left(1 + K^{*}_{M}\sigma^{2}_{I_{4\,M}}\right) \tag{7}$$

where $\bar{I}^{*}_{4\,,M}$ and $\sigma_{I_{4\,M}}$ are the average and the variance of the pseudo-invariant measuring the square of the stretch along any spatial direction of the M-th set of fibers, $k_{1\,M}$ is a stiffness parameter that controls the behavior of the fibers at small strains, $k_{2\,M}$ is a dimensionless rigidity parameter that controls the behavior of the fibrils at large strains, and K^{*}_{M} a coefficient dependent on $\bar{I}^{*}_{4\,,M}$, $k_{1\,M}$, and $k_{2\,M}$, cf.[23]

The number of parameters of the material model (seven) makes the search for the non-unique optimal set of parameters rather expensive from the numerical point of view. To illustrate the method, we reduce the problem to the same level of difficulty of the Mooney-Rivlin material model, by assigning the values of the penalty coefficient K and of the four fiber parameters $k_{1\,M}, k_{2\,M}$ according to the data documented in in Sánchez *et al.*[40] Therefore, we set $K = 5.5$ MPa, $k_{1\,1} = k_{1\,2} = 0.05$ MPa, and $k_{2\,1} = k_{2\,2} = 200$. Again, the baseline cornea labelled S1 has been used for demonstration. The search is conducted only on the shear stiffness parameters μ_1 and μ_2, adopting the same strategy described in Section 3.2.

The parameter μ_1 has been set as $\{0.04, 0.05, 0.06, 0.07\}$ MPa. The computed ML index as a function of $\mu_1 = \mu_2$ is shown in Figure 10(a). The optimal value of $\mu_1^{\mathrm{opt}} = 0.05$ MPa is clearly shown in the plot, with the corresponding ML index equal to 6.1114 $\times 10^{-6}$. The second search is conduced for $\mu_1^{\mathrm{opt}} = 0.05$ MPa, varying μ_2 in $\{0.03 - -0.07\}$ MPa. The dependence of the ML index on μ_2 is shown in Figure 10(b), and the optimal value is $\mu_2^{\mathrm{opt}} = 0.05$ MPa.

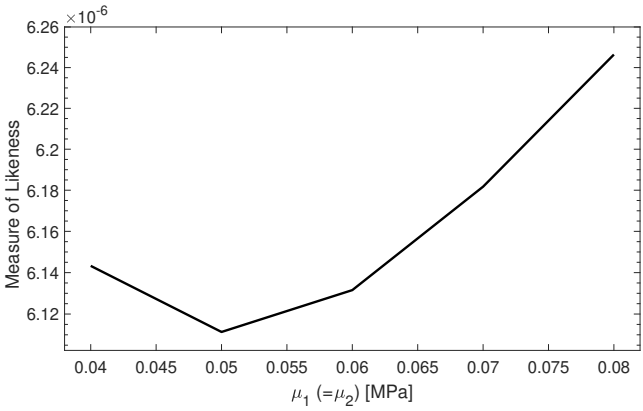

(a) First search

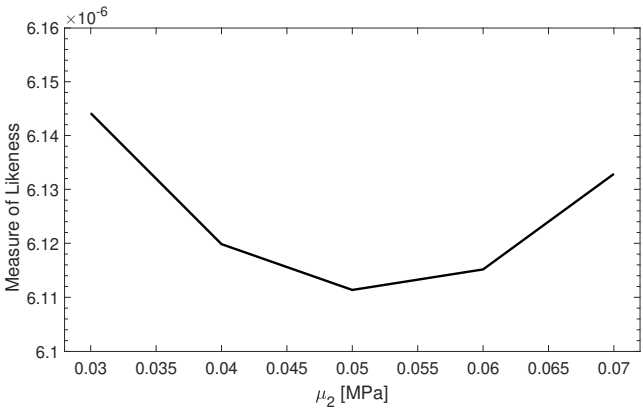

(b) Second search

Fig. 10. Baseline cornea with anisotropic distributed fiber reinforced material. (*a*) Dependence of the ML index on the first shear stiffness parameter μ_1, under the constraint $\mu_2 = \mu_1$. (*b*) Dependence of the ML index on the second shear stiffness parameter μ_2 for a fixed value $\mu_1 = 0.05$ MPa.

4. Discussion

We illustrated a procedure for the simultaneous identification of the stress-free geometry and a reduced set of material parameters for a patient-specific model of a human cornea that underwent laser ablation surgery (PRK). The identification procedure is specifically related to the availability of two comparable configurations, corresponding to a preoperative and a postoperative state, respectively.

The situation is not the ideal one, since the material properties can be identified

only after the surgery. Therefore the model cannot exploit its predictability in view of optimizing the ablation profile. Nevertheless, we have been motivated by several reasons to conduct this study.

First, the achieved patient-specific model could be employed to estimate the response of the eye to additional surgery, for example, the insertion of an intraocular lens or the execution of a crosslinking procedure. Second, the aim of this work is to describe a conceptually general procedure that can be modified and improved by the suitable selection of two or more comparative configurations of the same cornea, obtained with other means, for example, with a planned protocol of *in-vivo* tests. Third, the application of this approach to a large set of human corneas that have undergone PRK refractive surgery can be used to restrict the variability of the material parameters of different material models into physically significant ranges of values.

The proposed method must be intended as one of the several ways that allow to identify the material properties of an assigned material model. In particular, the method relies on the existence of an ideal stress-free configuration that cannot be attained under physiological conditions, because it is associated to a non-physiological state, at zero IOP. The ideal unstressed configuration can be determined only through numerical calculations conducted in finite kinematics. In fact, linear elastic approaches are based on the assumption that there is no change of configuration under loading, or no difference between he stress-free and the physiological configuration, excluding the possibility to use the method for the estimation of material parameters. Therefore, the proposed method is suitable only to finite kinematics material models that describe the behavior of deformable soft tissues.

To compensate the missing surrounding tissues, throughout the calculation we adopted special boundary conditions consisting in the adaptive rotation, *i. e.*, a driven motion of the nodes located at the limbus boundary to preserve the planarity of the boundary while enforcing the normality to the mid-surface of the deforming cornea. The concept of rotating boundaries has been presented in a previous study,[21] as an alternative to fixed boundary (mimicking rigid environment) and to elastic boundaries (mimicking by means of tuned springs the elasticity of surrounding tissues). With respect to other boundary conditions, the adaptive rotations of the limbus have been proven by means of comparative analyses to be the ones providing the most realistic refractive properties of the deforming cornea, showing the minimal variation of the refractive power with growing IOP and the lowest elastic energy stored in the system.

Among the methods proposed in the literature for the identification of the stress-free state, the approach proposed in Grytz and Downs,[14] where the concept of the comparison between distinct configurations is used to estimate the physiological stress/strain state in biological tissues, stands close to our previously described algorithm.[8] Although presented in a more formal and elegant way with respect to our work,[8] the underlying idea is the same: to reconstruct the physiological stress state by searching for a stress-free configuration. The difference between the two methods is that here we are comparing two configurations that differ for tissue mass and volume but withstand the same load, Grytz and Downs[14] compare two configu-

rations that differ for loads but preserve mass and volume.

The approach has been illustrated with reference to three material models: the Hooke extended to the non-linear range, the Mooney-Rivlin, and the anisotropic stochastic fiber reinforced model.[23] The first two material models, which are not particularly suitable for modelling the human corneas, have been considered in order to set up and verify the procedure. In particular, the Hooke model should not be used for soft tissues, since it overestimates the stiffness, and therefore the stress, within the tissue.

The advantages of using the Hooke model is related to the computational convenience in the solution of the elastic problem: the algorithm is rather fast and it has been possible to conduct numerous analyses considering twelve corneas. In this respect, it has been possible to observe that one of the key points in the procedure is the alignment of the corneas in order to allow the comparison. Specifically, images of the eye may be affected by some unavoidable change of reference system. Optical machines detect at best the NT direction, so that images are generally taken with a minimum difference in terms or rotation. However, misplacement in the optical axis directions is always possible. Thus, after creating of the solid model, it may be necessary to perform some additional relative roto-translation to minimize the geometrical differences. In our approach, we refer to the limbus geometry as the one that undergoes the minimum changes also after PRK surgery and conduct all sorts of re-alignment using the limbus as reference. The particular unsuccessful case of the cornea labelled 1D is exemplary in this regard. We believe that the images have been affected by some unwanted bias that we were not able to detect. Therefore, in general, it is important that the images are taken with the same tomographer operated by the same surgeon to minimize the differences.

The identified geometry and set of material properties obtained by the approach will be dependent also on the patient-specific IOP. In this study, we used an ideal IOP (14 mmHg) because this information was not available. The fact that the IOP was not patient-specific can also justify the fact that some corneas showed clear optimal parameter values, whereas for others the procedure failed. It is important to note that, in general, IOP measured by tonometers is biased due to corneal stiffness. Many tonomoters are based on correction tables, often based on a wide set of numerical calculations conducted on ideal corneas to provide a less biased indication of IOP. This expedient does not avoid to obtain the patient-specific IOP, but only an averaged value. We believe that IOP has to be considered as an unknown of the problem, and it must be identified, together with the stress-free geometry and material properties, in a more sophisticated inverse analysis, which is presently the object of a study in our group.

The difficulties observed in using unrealistic materials (Hooke and Mooney-Rivlin) for the identification of an anisotropic body are indeed less marked when a more accurate material model is selected, as it has been observed in our previous applications.[5,32,40] As matter of fact, the ML index plot is characterized by the presence of a well-identified minimum, with smaller values, in the anisotropic case.

This indicates that an accurate material model is the basis of any good numerical simulation.

A final comment must be given on the search approach used in this study, conducted in a rather rough way by varying slightly one of the material parameters at time, under some assumptions not really supported by clinical evidence. Thus, criticism can be raised for the choice of keeping Poisson's coefficient constant in the Hooke material model case, or in conducting two disjoined searches on a single parameter for the Mooney-Rivlin model case, or in excluding from the search the fibril stiffness and rigidity parameters for the anisotropic material model.

We are convinced that the optimization of the ML index must be conducted with more solid search algorithms, that include not only all the relevant material properties, but also the IOP as unknown action. The multi-objective search can be based on faster algorithms, typically used in inverse analysis, such as the conjugate gradient and methods based on Pareto optimality criteria.

References

1. Maurice DM. The structure and transparency of the cornea. J Physiol. 1957;136(2): 263–286.
2. Meek KM, Blamires T, Elliot GF, Gyi TJ, Nave C. The organization of collagen fibrils in the human corneal stroma: a synchroton x-ray diffraction study. Curr Eye Res. 1987;6, 841–846.
3. Daxer A, Fratzl P. Collagen fibril orientation in the human corneal stroma and its implication in keratoconus. Invest Ophthalmol Vis Sci. 1997;38, 121–129.
4. Munnerlyn CR, Koons SJ, Marshall J. Photorefractive keratectomy: a technique for laser refractive surgery. J Cataract Refract Surg. 1988;14(1): 46–52.
5. Simonini I, Pandolfi A. Customized finite element modelling of the human cornea. PLoS One. 2015;10(6): e0130426.
6. Boschetti F, Triacca V, Spinelli L, Pandolfi A. Mechanical Characterization of Porcine Corneas. J Biomech Eng. 2012;134(3): 031003–1–9.
7. Pinsky PM, Heide D van der, Chernyak D. Computational modeling of mechanical anisotropy in the cornea and sclera. J Cataract Refract Surg. 2005;31(1): 136–145.
8. Pandolfi A, Manganiello F. A material model for the human cornea. Biomech Model Mechanobiol. 2006;5, 237–246.
9. Aghamohammadzadeh H, Newton RH, Meek KM. X-ray scattering used to map the preferred collagen orientation in the human cornea and limbus. Structure. 2004;12(2): 249–256.
10. Quantock AJ, Boote C, Young RD, Hayes S, Tanioka H, Kawasaki S, et al. Small-angle fibre diffraction studies of corneal matrix structure: a depth-profiled investigation of the human eye-bank cornea. J Appl Crystallogr. 2007;40(s1): s335–s340.
11. Wollensak G, Spörl E, Mazzotta C, Kalinski T, Sel S. Interlamellar cohesion after corneal crosslinking using riboflavin and ultraviolet A light. Br J Ophthalmol. 2011;95(6): 876–880.
12. Petsche SJ, Chernyak D, Martiz J, Levenston ME, Pinsky PM. Depth-dependent transverse shear properties of the human corneal stroma. Invest Ophthalmol Vis Sci. 2012;53, 873–880.
13. Meek KM, Boote C. The use of X-ray scattering techniques to quantify the orientation and distribution of collagen in the corneal stroma. Prog Retin Eye Res. 2009;28(5): 369–392.
14. Grytz R, Downs JC. A forward incremental prestressing method with application to inverse parameter estimations and eye-specific simulations of posterior scleral shells. Comput Methods Appl Mech Eng. 2013;16(7): 768–780.

15. Raghavan ML, Ma B, Fillinger MF. Non-invasive determination of zero-pressure geometry of arterial aneurysms. Ann Biomed Eng. 2006;34(9): 1414–1419.
16. Bols J, Degroote J, Trachet B, Verhegghe B, Segers P, Vierendeels J. A computational method to assess the in vivo stresses and unloaded configuration of patient-specific blood vessels. J Comput Appl Math. 2013;246, 10–17.
17. Bols J, Degroote J, Trachet B, Verhegghe B, Segers P, Vierendeels J. Inverse modelling of image-based patient-specific blood vessels: zero-pressure geometry and in vivo stress incorporation. ESAIM: Math Model Num. 2013;47(4): 1059–1075.
18. Lu J, Zhou X, Raghavan ML. Inverse elastostatic stress analysis in pre-deformed biological structures: demonstration using abdominal aortic aneurysms. J Biomech. 2007;40(3): 693–696.
19. De Putter S, Wolters BJ, Rutten MC, Breeuwer M, Gerritsen FA, Vosse FN Van de. Patient-specific initial wall stress in abdominal aortic aneurysms with a backward incremental method. J Biomech. 2007;40(5): 1081–1090.
20. Gee MW, Reeps CH, Eckstein HH, Wall WA. Prestressing in finite deformation abdominal aortic aneurysm simulation. J Biomech. 2009;42(11): 1732–1739.
21. Pandolfi A, Holzapfel GA. Three-dimensional modelling and computational analysis of the human cornea considering distributed collagen fiber orientation. J Biomech Eng. 2008;130, 061006.
22. Pandolfi A, Fotia G, Manganiello F. Finite element simulations of laser refractive corneal surgery. Eng Comput. 2009;25(1): 15–24.
23. Pandolfi A, Vasta M. Fiber distributed hyperelastic modeling of biological tissues. Mech Mat. 2012;44, 151–162.
24. Ariza-Gracia MA, Zurita JF, Piñero DP, Rodriguez-Matas JF, Calvo B. Coupled biomechanical response of the cornea assessed by non-contact tonometry. A simulation study. PLoS One. 2015;10(3): e0121486.
25. Ariza-Gracia MÁ, Zurita J, Piñero DP, Calvo B, Rodriguez-Matas JF. Automatized patient-specific methodology for numerical determination of biomechanical corneal response. Ann Biomed Eng. 2016;44(5): 1753–1772.
26. Ariza-Gracia MÁ, Redondo S, Llorens DP, Calvo B, Rodriguez-Matas JF. A predictive tool for determining patient-specific mechanical properties of human corneal tissue. Comput Methods Appl Mech Eng. 2017;317, 226–247.
27. Ariza-Gracia MÁ, Wu W, Calvo B, Malvè M, Büchler P, Rodriguez-Matas JF. Fluid-structure simulation of a general non-contact tonometry. A required complexity? Comput Methods Appl Mech Eng. 2018;
28. Otani T, Tanaka M. Unloaded shape identification of human cornea by variational shape optimization. Comput Methods Biomech Biomed Engin. 2018; 1–8.
29. Wollensak G, Spöerl E, Seiler T. Stress-strain measurements of human and porcine corneas after riboflavin-ultraviolet-A-induced cross-linking. J Cataract Refract Surg. 2003;29, 1780–1785.
30. Elsheikh A. Finite Element Modeling of Corneal Biomechanical Behavior. J Refract Surg. 2010;26(4): 289–300.
31. Seven I, Vahdati A, De Stefano VS, Krueger RR, Dupps WJ. Comparison of patient-specific computational modeling predictions and clinical outcomes of LASIK for myopia. Invest Ophthalmol Vis Sci. 2016;57(14): 6287–6297.
32. Montanino A, Gizzi A, Vasta M, Angelillo M, Pandolfi A. Modeling the biomechanics of the human cornea accounting for local variations of the collagen fibril architecture. J Appl Math Mech. 2018;98(12): 2122–2134.
33. Studer H, Riedwyl H, Büchler P. Importance of multiple loading scenarios for the identification of material coefficients of the human cornea. Comput Methods Appl Mech Eng. 2012;15(1): 93–99.
34. Kok S, Botha N, Inglis HM. Calibrating corneal material model parameters using only inflation data: An ill-posed problem. Int J Numer Method Biomed Eng. 2014;30(12): 1460–1475.
35. Petsche SJ, Pinsky PM. The role of 3-D collagen organization in stromal elasticity: a model based on X-ray diffraction data and second harmonic-generated images. Biomech Model Mechan. 2013;12(6): 1101–1113.

36. Simonini I, Pandolfi A. The influence of intraocular pressure and air jet pressure on corneal contactless tonometry tests. J Mech Behav Biomed Mater. 2016;58, 75–89.
37. Simonini I, Angelillo M, Pandolfi A. Theoretical and numerical analysis of the corneal air puff test. J Mech Phys Solids. 2016;93, 118–134.
38. Montanino A, Angelillo M, Pandolfi A. Modelling with a meshfree approach the cornea-aqueous humor interaction during the air puff test. J Appl Math Mech. 2018;77, 205–216.
39. Montanino A, Angelillo M, Pandolfi A. A 3D fluid-structure interaction model of the air puff test in the human cornea. J Mech Behav Biomed Mater. 2019;94, 22–31.
40. Sánchez P, Moutsouris K, Pandolfi A. Biomechanical and optical behavior of human corneas before and after photorefractive keratectomy. J Cataract Refract Surg. 2014;40(6): 905–917.

© Journal for Modeling in Ophthalmology 2020; 4:34-43
Original article

Test-retest reproducibility of atomic force microscopy measurements of human trabecular meshwork stiffness

Larry Kagemann[1-8], Joe Candiello[2], Gadi Wollstein[1-4,6], Hiroshi Ishikawa[1-4,6,10], Richard A. Bilonick[1,3,11], Ian A. Sigal[1-4], Christian Jonescu-Cuypers[9], Prashant N. Kumta[2,3,12,13], Joel S. Schuman[1-4,6,10]

[1]UPMC Eye Center, Eye and Ear Institute, Ophthalmology and Visual Science Research Center, Department of Ophthalmology, University of Pittsburgh School of Medicine, Pittsburgh, PA, USA; [2]Department of Bioengineering, Swanson School of Engineering, University of Pittsburgh, Pittsburgh, PA, USA; [3]McGowan Institute for Regenerative Medicine, University of Pittsburgh School of Medicine and University of Pittsburgh, Pittsburgh, PA, USA; [4]The Louis J. Fox Center for Vision Restoration, University of Pittsburgh School of Medicine, Pittsburgh, PA, USA; [5]US Food and Drug Administration, Silver Spring, MD, USA; [6]NYU Langone Eye Center, NYU School of Medicine, New York University, New York, NY, USA; [7]Department of Ophthalmology, School of Medicine, University of Maryland, Baltimore, MD, USA; [8]Department of Surgery, Uniformed Services University of the Health Sciences, Bethesda, MD, USA; [9]Department of Ophthalmology, Geneva University Hospitals, Geneva, Switzerland; [10]Department of Biomedical Engineering, NYU Tandon School of Engineering, Brooklyn, NY, USA; [11]Department of Biostatistics, Graduate School of Public Health, University of Pittsburgh, Pittsburgh, PA, USA; [12]Department of Chemical and Petroleum Engineering, University of Pittsburgh, Pittsburgh, PA, USA; [13]Department of Mechanical Engineering and Materials Science, University of Pittsburgh, Pittsburgh, PA, USA

Abstract

Purpose: The purpose of the present study was to quantify test-retest reproducibility of measurements of stiffness of the human trabecular meshwork (HTM) by atomic

Correspondence: Larry Kagemann, Ph.D., RAC, FARVO, US Food and Drug Administration, White Oak Building 66, Room 1252, 10903 New Hampshire Avenue, Silver Spring, MD 20993-0002, USA.
E-mail: Lawrence.Kagemann@fda.hhs.gov

force microscopy (AFM).
Methods: Eleven 40 µm radial limbal cryostat sections from a fresh human donor rim were mounted on charged slides and rehydrated at room temperature. Stiffness at four TM locations (anterior to posterior along Schlemm's canal) was measured by AFM. At each location, a 6 x 6 grid was sampled. Indentation points were evenly distributed over a 20 µm x 20 µm area, with a rate of one load/unload cycle per second. Measurements were then repeated for calculation of test-retest variability.
Results: The test-retest coefficients of variation for the four measurement locations (anterior to posterior) were 24.39, 25.28, 12.74, and 14.26%, respectively, with a notable drop in the two posterior locations compared to the anterior. The test-retest coefficient for the sections was 19.17%. For the entire eye, the test-retest coefficient of variation for the measurement of the TM stiffness was 17.13%. Young's moduli consistently decreased from anterior to posterior location.
Conclusions: Wide regional variation suggests that single value does little to fully describe the complex array of TM stiffness levels within the eye, and future studies of TM stiffness assessed by AFM should include multiple tissue samples from each eye, with documentation of the anterior-posterior location of each measurement.

1. Introduction

Elevated intraocular pressure (IOP) is the single most important risk factor in the diagnosis[1-3] and progression[4,5] of glaucoma, and its reduction is the single clinical endpoint of treatment.[6] Overby *et al.* recently demonstrated that gene expression in glaucoma is altered, resulting in elevated stiffening of the inner wall of Schlemm's canal, impeding formation of pores, leading to IOP elevation in glaucomatous eyes. To that end, there is increasing interest in the measurement of the stiffness of tissues in the proximal aqueous humor outflow pathway, including Schlemm's canal and the trabecular meshwork (TM).[7-13]

A study by Last *et al.* suggests that TM stiffness is increased in glaucoma.[7] In that study, stiffness (Young's modulus, E) as measured by atomic force microscopy (AFM) was found to vary by *two orders of magnitude* within individuals, and amongst subjects. AFM measurements of rat TM found that mean local stiffness changes by more than *twenty-fold* within *individual eyes*.[11]

We have successfully used AFM to quantify the stiffness of the basement membrane of the eye, but have not yet applied it to assess the measurement of TM stiffness.[14,15] AFM is known to be a noisy measurement,[16-22] although the test-retest reproducibility, *i.e.* the variation associated with repeated measurements of AFM assessment of TM stiffness, has not yet been quantified. The meaningful application of any technique to medical research first requires characterization of measurement error. The purpose of the present study was to quantify test-retest reproducibility of the human TM by AFM.

2. Methods

The study was conducted in accordance with the tenets of the Declaration of Helsinki and the United States Health Insurance Portability and Accountability Act.

A right eye was obtained from a local eye bank (Center for Organ Recovery, and Education, Pittsburgh, PA, USA). The donor eye was from a 53-year-old female, and tested negative for HIV I/II plus O, HBcAb, HCV/HIV/HB/Nat, RPR. The eye was harvested and preserved by the eye bank at ten hours after death. Specifically, the eye was stored in Optisol (Chiron Ophthalmics, Irvine, CA, USA) at -8 °C. Seven days after harvest, the cornea was removed for transplant and the rim was dissected and embedded in Tissue Tek Optimal Cutting Temperature Compound (Sakura Finetek USA Inc., Torrance, CA, USA) and stored at -80 °C. Radial 40 µm thick sections were cut on a cryostat (Leica CM3050 S cryostat, Leica Microsystems Inc., Buffalo Grove, IL, USA) and mounted on charged slides by an histotechnologist certified by the American Society for Clinical Pathology (ASCP).

TM stiffness was quantified by AFM standard accepted methods.[14,23,24] Briefly, 11 tissue sections were reconstituted with phosphate-buffered saline (PBS) and allowed to rest at room temperature for 20 minutes. The slide was then placed in a MFP-3D-BIO Atomic Force Microscope (Asylum Research, Santa Barbara, CA, USA) mounted on an Olympus IX-71 fluorescence microscope (Olympus, Tokyo, Japan). Standard commercially available 100 µm long Si3N4 cantilevers, with integrated pyramidal tips (Veeco, Inc, Santa Barbara, CA, USA) and a nominal spring constant (k) of 0.6 N/m were used to indent the TM cells, calibrating the spring constant of each cantilever before each experiment. A 6 x 6 grid was sampled, with indentation points evenly distributed over a 20 µm x 20 µm area. The measurement grid was applied in each of four areas (Fig. 1), with the AFM controlled by an automated process, at a rate of one load/unload cycle per second. The speed of the AFM tip indenting the tissue ranged from 2–10 µm/sec. The apparent Young's modulus of the tissue at each indentation point was calculated for each independent force-indentation curve using the Sneddon model.[25] After completing measurements at each of the four areas (session A), the slide was removed and repositioned in the AFM microscope, and all measurements were repeated (session B) to quantify test-retest reproducibility.

Stiffness estimates were acquired at 4 locations in each of the tissue sections (Fig. 1). Each stiffness estimate was comprised of the average of 36 (6 x 6 grid, 20 µm x 20 µm) individual measurements. This methodology is a standard tissue-sampling technique, and offered as a default setting in our commercially available AFM unit. Test-retest coefficient of variability was calculated for each of the four measurement locations. The average of the four stiffness measurements was calculated to provide a mean stiffness for each section, and the test-retest coefficient of variability was calculated for the sections. Finally, the 11 tissue stiffness estimates were averaged to estimate TM stiffness for the eye. These values were calculated for both AFM runs (session A and session B).

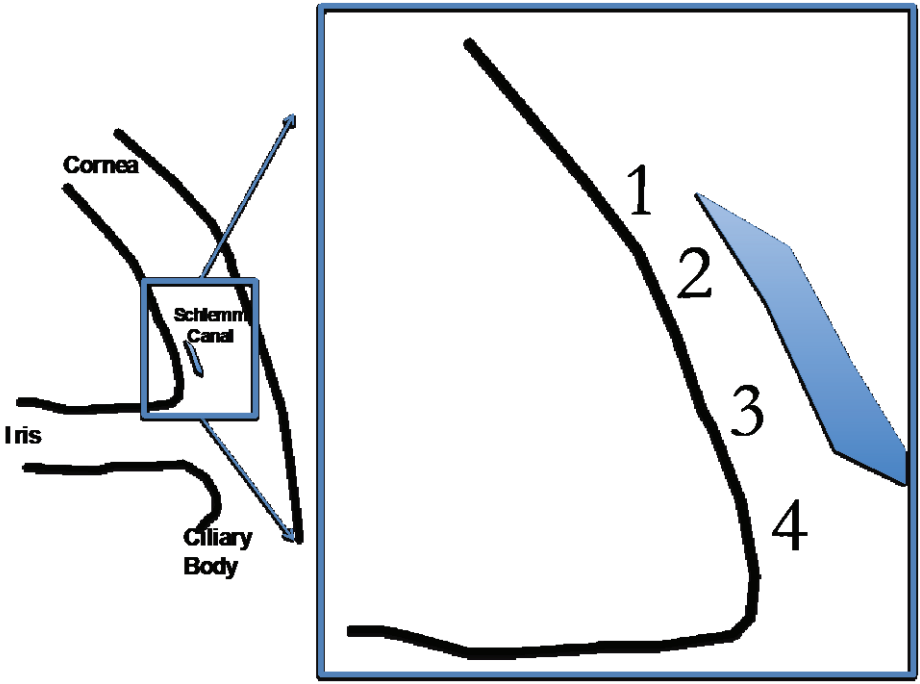

Fig. 1. The TM was measured at four locations from anterior to (*1*), adjacent to (*2, 3*), and posterior to (*4*) Schlemm's canal. Measurements at each location were obtained in sessions A and B.

3. Results

The overall range of Young's moduli in sessions A and B were 8,376–242,733 and 5,574–130,352 Pa, respectively (Table 1). Moving from location 1 to 4, Young's moduli consistently decreased during both measurements A and B. However, the location-to-location positional drop in Young's modulus was approximately 15 kPa larger in session A compared to session B (13.4 kPa to 15.7 kPa, Fig. 2). The pattern of anterior to posterior TM softening (Fig. 2) was present throughout the series of 11 tissue slabs.

The test-retest coefficients of variation for the four measurement locations (anterior to posterior) were 24.39, 25.28, 12.74, and 14.26%, respectively, with a notable drop in the two posterior locations compared to the anterior. The test-retest coefficient for the sections was 19.17% (Table 1). For the entire eye, the test-retest coefficient of variation for the measurement of the TM stiffness was 17.13%.

Table 1. Mean and standard deviation stiffness measurements from sessions A and B for the 11 tissue sections, with coefficients of variation for each tissue section, the mean of the tissue sections, and the eye overall

Section	Session A (Pa)	Session B (Pa)	Coefficient of variation
1	15,721 ± 9,434	17,589 ± 5,833	8%
2	8,376 ± 5,573	5,574 ± 2,684	28%
3	31,649 ± 5,485	17,779 ± 16,624	40%
4	32,586 ± 21,439	38,652 ± 17,250	12%
5	25,424 ± 7,478	27,116 ± 12,020	5%
6	35,368 ± 37,272	38,687 ± 17,250	6%
7	38,977 ± 38,589	32,744 ± 25,720	12%
8	220,012 ± 273,144	130,352 ± 108,487	36%
9	49,262 ± 58,909	58,294 ± 68,575	12%
10	242,733 ± 204,551	126,484 ± 89,613	45%
11	83,345 ± 39,141	120,895 ± 90,862	26%
Section mean	71,223 ± 63,720	55,833 ± 43,155	**17%**
Whole eye		63,528 ± 53,438	**21%**

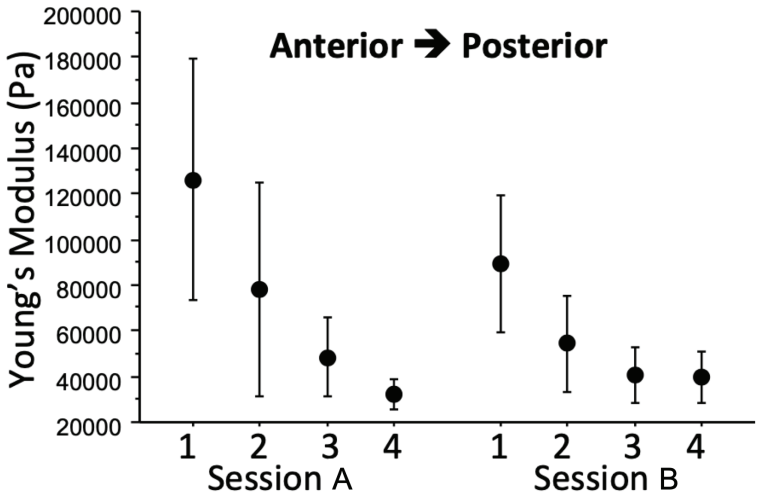

Fig. 2. Young's modulus presented with a trend of decrease with changing position from anterior to posterior locations in both sessions A and B; however, there were no statistically significant differences observed between the locations.

4. Discussion

To date, published estimates of TM stiffness measured by AFM are comprised of single averages used to represent an entire eye.[7,8,10] They present with variability greater than two orders of magnitude. The magnitude of the variability is unexplained, leaving the reader to speculate if its source is measurement error, true difference between sections, or true differences within the sections and between subjects. For example, the ranges of tissue stiffnesses (in kPa) in glaucomatous eyes, by subject, were 1.4–329.7, 36.4–382.8, 1.7–565.3, 0.8–552.0, 23.2–126.6, 0.5–206.9, 2.0–243.0, 1.3–315.8, 5.3–178.5, and 1.5–142.5.[7] The present study provides the first systemic examination of the sources of variability in AFM measurements of TM stiffness. We found that AFM had a test-retest coefficient of variation 17% in an eye, and 19% for any individual tissue section. Further, we found that TM stiffness decreased with position from anterior to posterior.

A closer examination of the individual measurements suggests that the majority of test-retest discordance occurs in regions of high stiffness (Fig. 3). This may suggest that those anterior regions adjacent to the sclera (regions 1 and 2) contain a wider variety of small and large TM stiffness, unlike the posterior (regions 3 and 4), which present with relatively smaller levels of measurement variability (Fig. 2). Indeed, the large differences in those measurement locations with the highest stiffness values (Fig. 3) suggest a “hit or miss” phenomenon with respect to local regions of high stiffness, especially in the anterior-most location 1. These data suggest that the

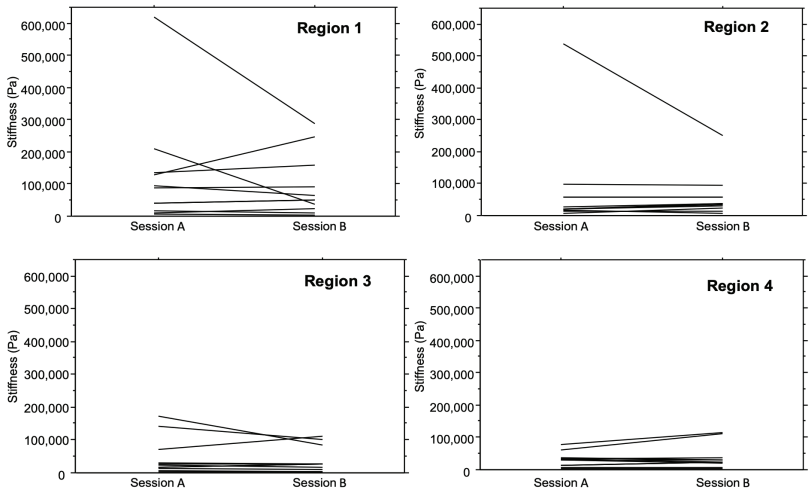

Fig. 3. Individual variation between the two sessions was small, with the exception of a small number of outliers in each region. Note that, in each case, large variability occurred in sections with high stiffness.

most stable AFM measurements are to be found in the softer posterior-most region of the TM (Figs. 2 and 3). However, limiting assessment to the softest region of the TM, by definition, biases the measurements to lower values.

The establishment of the level of measurement noise is necessary for power calculations in future studies. The present data also provides some insights into the reality of expected variability within individual tissue sections and individual eyes. The unexpected finding of a predictable pattern of regional variation within individual tissue slices, representing a predictable "normal" pattern of TM softening deep within the angle, may in itself serve as a biomarker for disease. However, in the present study, the tissue was completely relaxed, having been sectioned from a donor eye. It is possible that this pattern may be altered in living eyes due to the influence of muscle activity within the TM itself, as well as via influence of ciliary muscle activity transmitted to the TM via connecting tendons.

Regional differences throughout the eye suggest a need for a comprehensive assessment of TM stiffness. We do not yet fully understand the relationship between varied levels of TM stiffness and regional outflow. However, the presence of softer TM in the posterior location is consistent with histological observations in older eyes, specifically of pigment deposition in the TM adjacent to Schlemm's canal, but not anterior, marking posterior TM as the area of active flow.[26] In this study, we found the posterior TM to have lower stiffness, also consistent with the hypothesis that regions of active outflow have lower TM stiffness.

The present study has several limitations. As the primary purpose of the study was to determine expected variability when measuring TM stiffness in a single eye, multiple sections from only one eye were used. Data from one eye are not generalizable to the population, and further studies are needed. However, the pattern observed in this human donor eye agrees with previous published findings in a rodent model.[11] Surprisingly, despite measuring stiffness from an individual eye, the present study demonstrated that a wide range of stiffness values is present in an eye. Until we better understand the meaning of this range of values, an individual mean may not adequately quantify TM stiffness. The data suggest that tissue samples from numerous locations around the TM are needed, and within each sample, the anterior-posterior location should be documented. Further, in the present study, a pyramidal-tipped AFM probe was used. These tips are known to yield higher estimations of cell stiffness than spherical tips, but are valid for measurements in soft tissue.[27] Previous studies have elected to use a probe with a spherical tip.[7] The use of a pyramidal tip may yield stiffness estimates more affected by the TM cell cortex, but stiffness estimates in the present study ranged from a few to several hundred kilopascals; far larger than the small differences observed when comparing spherical and "sharp" AFM probe tips.[28] There was good agreement between the first and second measurements of the tissue slices, suggesting that the performance of the pyramidal tipped AFM probe was reproducible (Fig 3). Finally, rehydrated tissue sections were used in the present study, as opposed to fresh

whole-tissue sections. This is an accepted and previously published technique in the measurement of stiffness of the biological ophthalmic structures.[23,24]

AFM reveals local patterns of TM stiffness in the human eye. The relationship between this array of stiffness levels, morphology, and outflow has yet to be determined in either cadaveric flow models, or more importantly, in living healthy and glaucomatous eyes. Wide regional variation suggests that single value does little to fully describe the complex array of TM stiffness levels within the eye, and future studies of TM stiffness assessed by AFM should include multiple tissue samples from each eye, with documentation of the anterior-posterior location of each measurement.

Acknowledgements

Dr. Joel S. Schuman wishes to disclose that he received royalties for intellectual property licensed by the Massachusetts Institute of Technology and Massachusetts Eye and Ear Infirmary to Zeiss, Inc.

Dr. Prashant N. Kumta acknowledges the Edward R. Weidlein Chair Professorship and the Center for Complex Engineered Multi-functional Materials (CCEMM), Swanson School of Engineering, University of Pittsburgh for use of the AFM.

The contents of this publication are the sole responsibility of the author(s) and do not necessarily reflect the views, opinions, or policies of Uniformed Services University of the Health Sciences (USUHS), the US Food and Drug Administration, the Department of Defense (DoD), the Departments of the Army, Navy, or Air Force. Mention of trade names, commercial products, or organizations does not imply endorsement by the US Government.

This work was supported in part by National Institutes of Health (Bethesda, MD, USA) contracts R01-EY13178, and P30-EY08098, the Eye and Ear Foundation (Pittsburgh, PA, USA), and unrestricted grants from Research to Prevent Blindness (New York, NY, USA).

References

1. Leske MC, Connell AM, Schachat AP, Hyman L. The Barbados Eye Study. Prevalence of open angle glaucoma. Arch Ophthalmol. 1994;112:821-829.
2. Mitchell P, Smith W, Attebo K, Healey PR. Prevalence of open-angle glaucoma in Australia. The Blue Mountains Eye Study. Ophthalmology. 1996;103:1661-1669.
3. Sommer A, Tielsch JM. Risk factors for open-angle glaucoma: the Barbados Eye Study. Arch Ophthalmol. 1996;114:235.

4. Drance S, Anderson DR, Schulzer M, Collaborative Normal-Tension Glaucoma Study G. Risk factors for progression of visual field abnormalities in normal-tension glaucoma. Am J Ophthalmol. 2001;131:699-708.
5. Leske MC, Hyman L, Hussein M, Heijl A, Bengtsson B. Comparison of glaucomatous progression between untreated patients with normal-tension glaucoma and patients with therapeutically reduced intraocular pressures. The effectiveness of intraocular pressure reduction in the treatment of normal-tension glaucoma. Am J Ophthalmol. 1999;127:625-626.
6. American Academy of Ophthalmology, Glaucoma Panel, Preferred Practice Pattern Guidelines. Primary Open-Angle Glaucoma. San Francisco CA, AAO. 2010.
7. Last JA, Pan T, Ding Y, et al. Elastic modulus determination of normal and glaucomatous human trabecular meshwork. Invest Ophthalmol Vis Sci. 2011;52:2147-2152.
8. Camras LJ, Stamer WD, Epstein D, Gonzalez P, Yuan F. Differential effects of trabecular meshwork stiffness on outflow facility in normal human and porcine eyes. Invest Ophthalmol Vis Sci. 2012;53:5242-5250.
9. Yu JG, Bao FJ, Feng YF, et al. Assessment of corneal biomechanical behavior under posterior and anterior pressure. J Refract Surg. 2013;29:64-70.
10. Camras LJ, Stamer WD, Epstein D, Gonzalez P, Yuan F. Circumferential tensile stiffness of glaucomatous trabecular meshwork. Invest Ophthalmol Vis Sci. 2014;55:814-823.
11. Huang J, Camras LJ, Yuan F. Mechanical analysis of rat trabecular meshwork. Soft Matter. 2015;11(14):2857-2865.
12. Morgan JT, Raghunathan VK, Chang YR, Murphy CJ, Russell P. The intrinsic stiffness of human trabecular meshwork cells increases with senescence. Oncotarget. 2015.
13. Morgan JT, Raghunathan VK, Chang YR, Murphy CJ, Russell P. Wnt inhibition induces persistent increases in intrinsic stiffness of human trabecular meshwork cells. Exp Eye Res. 2015;132:174-178.
14. Candiello J, Balasubramani M, Schreiber EM, et al. Biomechanical properties of native basement membranes. FEBS J. 2007;274:2897-2908.
15. Candiello J, Cole GJ, Halfter W. Age-dependent changes in the structure, composition and biophysical properties of a human basement membrane. Matrix Biol. 2010;29:402-410.
16. Ruozi B, Tosi G, Forni F, Fresta M, Vandelli MA. Atomic force microscopy and photon correlation spectroscopy: two techniques for rapid characterization of liposomes. Eur J Pharm Sci. 2005;25:81-89.
17. Trache A, Meininger GA. Atomic force-multi-optical imaging integrated microscope for monitoring molecular dynamics in live cells. J Biomed Optics. 2005;10:064023.
18. Tocha E, Schonherr H, Vancso GJ. Quantitative nanotribology by AFM: a novel universal calibration platform. Langmuir. 2006;22:2340-2350.
19. Tsuji T, Kobari K, Ide S, Yamanaka K. Suppression of spurious vibration of cantilever in atomic force microscopy by enhancement of bending rigidity of cantilever chip substrate. Rev Sci Instrum. 2007;78:103703.
20. Ying ZC, Reitsma MG, Gates RS. Direct measurement of cantilever spring constants and correction for cantilever irregularities using an instrumented indenter. Rev Sci Instrum. 2007;78:063708.
21. Akrami SM, Nakayachi H, Watanabe-Nakayama T, Asakawa H, Fukuma T. Significant improvements in stability and reproducibility of atomic-scale atomic force microscopy in liquid. Nanotechnology. 2014;25:455701.

22. Demichelis A, Divieto C, Mortati L, Pavarelli S, Sassi G, Sassi MP. Toward the realization of reproducible Atomic Force Microscopy measurements of elastic modulus in biological samples. J Biomech. 2015;48:1099-1104.
23. Braunsmann C, Hammer CM, Rheinlaender J, Kruse FE, Schaffer TE, Schlotzer-Schrehardt U. Evaluation of lamina cribrosa and peripapillary sclera stiffness in pseudoexfoliation and normal eyes by atomic force microscopy. Invest Ophthalmol Vis Sci. 2012;53:2960-2967.
24. Marturano JE, Arena JD, Schiller ZA, Georgakoudi I, Kuo CK. Characterization of mechanical and biochemical properties of developing embryonic tendon. Proc Natl Acad Sci U S A. 2013;110:6370-6375.
25. Radmacher M, Fritz M, Hansma PK. Imaging soft samples with the atomic force microscope: gelatin in water and propanol. Biophys J. 1995;69:264-270.
26. Freddo T, Johnson M. Aqueous Humor Dynamics I: Measurement methods and animal studies. In: Civan MM (ed), The Eye's Aqueous Humor. Amsterdam, Boston, Heidelberg, London, New York, Oxford, Paris, San Diego, San Francisco, Singapore, Sydney, Tokyo: Elsevier; 2008.
27. Harris AR, Charras GT. Experimental validation of atomic force microscopy-based cell elasticity measurements. Nanotechnology. 2011;22:345102.
28. Vargas-Pinto R, Gong H, Vahabikashi A, Johnson M. The effect of the endothelial cell cortex on atomic force microscopy measurements. Biophys J. 2013;105:300-309.

© Journal for Modeling in Ophthalmology 2020; 4:44-54
Original article

Effect of iStent Trabecular Micro-Bypass device on outflow system morphology

Nicholas Hess[1], Nisreen Mesiwala[1], Catherine Marando[2], Richard A. Bilonick[1,3], Leonard K. Seibold[2], Joel S. Schuman[1,4-6,8,10], Gadi Wollstein[1,4-6,8], Hiroshi Ishikawa[1,4-6,8,10], Ian A. Sigal[1,4-6], Ian Conner[1,4-6], Christian Jonescu-Cuypers[9], Mina B. Pantcheva[2], Larry Kagemann[1,4-8,11,12]

[1]UPMC Eye Center, Eye and Ear Institute, Ophthalmology and Visual Science Research Center, Department of Ophthalmology, University of Pittsburgh School of Medicine, Pittsburgh, PA, USA; [2]Department of Ophthalmology, The Rocky Mountain Lions Eye Institute, University of Colorado Health Sciences Center, Aurora, CO, USA; [3]Department of Biostatistics, Graduate School of Public Health, University of Pittsburgh, Pittsburgh, PA, USA; [4]Department of Bioengineering, Swanson School of Engineering, University of Pittsburgh, Pittsburgh, PA, USA; [5]McGowan Institute for Regenerative Medicine, University of Pittsburgh School of Medicine and University of Pittsburgh, Pittsburgh, PA, USA; [6]The Louis J. Fox Center for Vision Restoration, University of Pittsburgh School of Medicine, Pittsburgh, PA, USA; [7]US Food and Drug Administration, Silver Spring, MD, USA; [8]NYU Langone Eye Center, NYU School of Medicine, New York University, New York, NY, USA; [9]Department of Ophthalmology, Geneva University Hospitals, Geneva, Switzerland; [10]Department of Biomedical Engineering, NYU Tandon School of Engineering, Brooklyn, NY, USA; [11]Department of Ophthalmology, School of Medicine, University of Maryland, Baltimore, MD, USA; [12]Department of Surgery, Uniformed Services University of the Health Sciences, Bethesda, MD, USA

Abstract

Purpose: Rigorous clinical testing has established that Schlemm's canal cross-sectional area (SC-CSA) is reduced in glaucomatous eyes. However, to date, it is unclear whether trabecular bypass procedures impact the morphology of the proximal aqueous outflow tract, or if the introduction of a local region of low outflow resistance

Correspondence: Larry Kagemann, PhD, RAC, FARVO, US Food and Drug Administration, White Oak Building 66, Room 1252, 10903 New Hampshire Avenue, Silver Spring, MD 20993-0002, USA.
E-mail: Lawrence.Kagemann@fda.hhs.gov

adversely affects SC-CSA elsewhere, specifically presenting as SC diminution. This study quantifies changes in the morphology of the distal outflow pathway after iStent Trabecular Micro-Bypass stent (Glaukos Corp, Laguna Hills, CA, USA) implantation in living eyes by anterior segment optical coherence tomography (OCT).
Design: This was a prospective observational study.
Subjects: This study included six patients (eight eyes) with primary-open angle glaucoma.
Methods: Patients underwent iStent placement in the nasal anterior chamber angle quadrant. OCT imaging was obtained of both nasal and temporal eye quadrants before and after surgery. For each SC parameter, an average of ten consecutive, evenly spaced measurements were manually obtained over a 1 mm segment of SC on FIJI ImageJ. Linear mixed effects modeling quantified the effect of the iStent on these parameters.
Main outcome measures: Main outcome measures were changes in SC-CSA, inner-to-outer wall distance (IOD), and trabecular meshwork (TM) thickness following iStent placement.
Results: Following iStent placement, total SC-CSA increased an average of 1,039.12 μm^2 ($P = 0.05$). Individually, there were no significant changes in SC-CSA in the nasal or temporal quadrants. Total SC-IOD and nasal SC-IOD increased an average of 2.35 µm ($P = 0.01$) and 2.96 µm ($P = 0.04$), respectively. There were no significant changes in temporal quadrant SC-IOD. There were no significant changes in TM thickness in either quadrant.
Conclusions: Implantation of the iStent Trabecular Micro-Bypass stent significantly increases SC-IOD in the nasal quadrant at the location of implant, with no evidence of SC diminution in the temporal quadrant. It remains unclear how these observations relate to the surgical efficacy of trabecular bypass procedures.

Keywords: glaucoma, iStent, outflow, Schlemm's canal, trabecular meshwork

1. Introduction

Glaucoma is the second leading cause of irreversible blindness in the world.[1] While elevated intraocular pressure (IOP) is a known risk factor for the development and progression of this disease,[2-7] changes in eye morphology have also been observed. IOP is maintained through a tightly regulated equilibrium of aqueous humor formation and elimination.[8] Aqueous humor is eliminated from the anterior chamber of the eye through an outflow system consisting of the trabecular meshwork (TM), Schlemm's canal (SC), and aqueous vasculature (veins and collector channels), and lastly, scleral veins connecting to the venous circulation.[9] In the presence of glaucoma, critical outflow structures appear to narrow,[10] which may alter the eye's ability for aqueous humor elimination.

In normal eyes, the location of greatest resistance to outflow is the juxtacanalicular tissue and inner wall of SC, the interface between SC and the TM.[11,12] In recent years, surgically-inserted micro-bypass devices such as the iStent (Glaukos Corp, Laguna Hills, CA, USA) have been shown to effectively lower IOP.[13-18] This L-shaped device, typically inserted in the nasal quadrant, transverses the juxtacanalicular tissue and TM and is believed to create a low-resistance channel between the anterior chamber and SC. This low-resistance channel increases aqueous humor outflow, and decreases IOP as a result. While it is likely that insertion of the iStent will alter the morphology of SC at the site of implantation, introduction of a localized low-resistance outflow pathway may alter the morphology of the SC elsewhere in the eye as the pattern of outflow is altered.

Previously, we have been able to image the primary aqueous humor outflow system in living human eyes, and observe decreased SC cross-sectional area (SC-CSA) in response to acutely elevated IOP.[19-21] Furthermore, the SC-CSA is known to decrease in patients with primary open-angle glaucoma.[10,22,23] It is not known if iStent insertion relieves SC-CSA diminution at the site or implant, or, exacerbates it elsewhere. The purpose of this study was to investigate the effects of iStent insertion on outflow system morphology using spectral domain optical coherence tomography (SD-OCT Bioptigen, Research Triangle Park, NC, USA), both at the site of implantation within the nasal quadrant, and in the opposing temporal quadrant.

2. Methods

All subjects were recruited in accordance with the tenets of the Declaration of Helsinki and the United States Health Insurance Portability and Accountability Act. This study was approved by the institutional review board of the University of Colorado (CO, USA), and all subjects provided written informed consent prior to participation.

2.1 Subjects

Subjects were enrolled at the University of Colorado Eye Center. Patients undergoing placement of iStent Trabecular Micro-Bypass device for primary open-angle glaucoma were recruited for this study. Subjects were imaged by SD-OCT before and after iStent. Images were obtained from both the nasal quadrant adjacent to iStent insertion, and also the temporal quadrant 180° from the insertion site. With the exception of one patient, all postoperative images were obtained within the one-month postoperative period.

2.2. iStent placement

All iStent insertions in this series were performed by glaucoma surgeons on the faculty of The Rocky Mountain Lions Eye Institute, University of Colorado Health

Sciences Center. Phacoemulsification with intraocular lens implantation was performed through a temporal corneal incision, with subsequent implantation of the iStent device in the nasal quadrant. The device was introduced through the temporal corneal incision and inserted through the TM and into SC via *ab interno* gonioscopy guidance. iStent was placed in the nasal quadrant in each eye; at the 3-4 o'clock position in right eyes and at 8-9 o'clock in left eyes.

2.3. Measurement of SC parameters

To ensure image consistency, all SD-OCT images were obtained in an office setting within the University of Colorado Eye Center and using the same scanner. Nasal and temporal quadrants were both imaged before and after iStent placement. Images were subsequently processed using 3D neighborhood averaging and contrast limited adaptive histogram equalization to improve discriminative resolution of SC and other outflow structures.[24] To account for variability of SC and outflow structure morphology, each measured parameter was obtained by taking an average of 10 consecutive, evenly spaced, measurements over a 1 mm segment of each 4 mm scan. Parameters were measured using FIJI (ImageJ, http://imagej.nih.gov/ij) image-processing software.

To measure TM thickness, we employed a previously described technique of fitting three perpendicular measurements from the anterior, middle, and posterior aspects of SC to the anterior chamber.[25] These three measurements were averaged, producing one measurement of TM thickness. SC-CSA was measured via manual segmentation,[20] and SC length was measured via a single linear measurement of the SC anterior-posterior axis (Fig. 1). Lastly, SC inner-to-outer wall distance (SC-IOD)

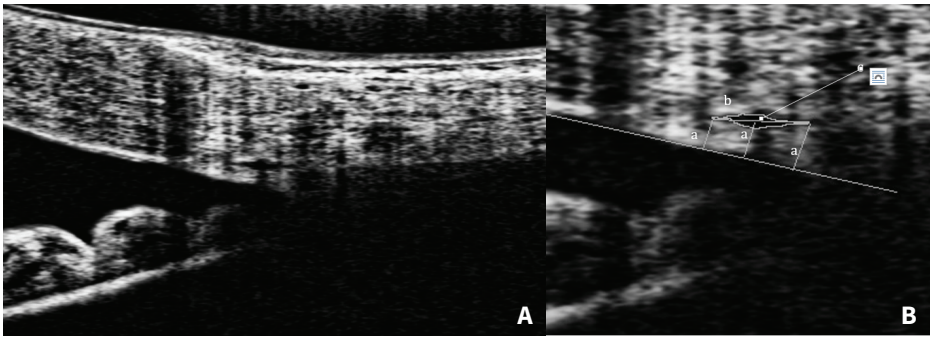

Fig. 1. (*A*) SD-OCT image of a living human eye. (*B*) Measurement of SC parameters: (*a*) three perpendicular measurements of TM thickness from anterior, middle, and posterior of SC to the anterior chamber; (*b*) SC-CSA; and (*c*) SC length measured via linear measurement of SC anterior-posterior axis.

was calculated by dividing SC-CSA by SC length. Complete blinding of the measuring process was not possible, as the iStent device was visible in postoperative scans of the nasal quadrant.

2.4. Statistical analysis

Statistical analysis was performed using the R Language and Environment for Statistical Computing software (version 3.2.2). Preoperative and postoperative SC and TM parameters were compared using a linear mixed-effects model. Separate comparisons were made for both the nasal and temporal quadrants. To compare an average outflow response across the limbus, a total value of each preoperative and postoperative parameter was also calculated. Continuous variables were compared using paired t-test. Statistical significance was defined as $P < 0.05$.

3. Results

Eight eyes from six patients with primary open-angle glaucoma were included in the analysis, four female and two male. Mean patient age was 75.5 years (range: 65 to 90 years). Patients underwent iStent placement between October 2012 and August 2014. Preoperative imaging was obtained a median of 7 days prior to surgery (range: 0 days to 31 days), and postoperative imaging was obtained a median of 8 days after surgery (range: 1 to 50 days).

3.1. IOP and medications

Median IOP and number of ocular anti-hypertensive medications did not vary considerably throughout the study period (Table 1). One patient (1 eye) failed to return for IOP measurements at months 3, 6, and 12.

3.2. TM thickness

There was no consistent change in TM thickness following iStent insertion. No significant change in TM thickness was observed in either the nasal or temporal quadrant, and likewise there was no significant change in overall total TM thickness (Table 2).

Table 1. Patient response to iStent insertion over one year

	Pre-iStent n = 6 (8 eyes)	**1 Week** n = 6 (8 eyes)	**3 Months** n = 5 (7 eyes)	**6 Months** n = 5 (7 eyes)	**1 Year** n = 5 (7 eyes)
IOP, median (range)	12 (11-15)	13.5 (11-22)	11 (8-14)	13 (8-22)	13 (9-14)
Medications, median (range)	2 (1-3)	--	1 (0-3)	1 (0-3)	1 (0-3)

IOP: intraocular pressure

Table 2. Changes in SC and TM morphology following iStent placement

	Pre-iStent	Post-iStent	Mean difference
SC-CSA, mean (SD), μ²			
Total	3,321.08 (1,464.66)	4,570.92 (1,212.91)	1,039.12#
Nasal	3,398.39 (1,136.91)	4,743.45 (1,323.24)	1,345.06
Temporal	3,242.76 (1,847.33)	4,312.14 (1,160.34)	580.22
SC length, mean (SD), μ			
Total	226.68 (51.80)	264.30 (54.17)	29.20
Nasal	248.79 (27.04)	285.03 (53.00)	36.24
Temporal	204.57 (63.23)	233.20 (44.41)	18.63
TM thickness, mean (SD), μ			
Total	187.51 (69.46)	222.29 (119.20)	24.41
Nasal	180.83 (52.73)	247.29 (142.66)	66.46
Temporal	194.20 (87.90)	184.78 (74.72)	-38.68
SC-IOD, mean (SD), μ			
Total	14.37 (3.63)	17.18 (2.51)	2.35*
Nasal	13.47 (3.23)	16.43 (2.67)	2.96†
Temporal	15.26 (4.08)	18.32 (2.05)	1.45

CSA: cross-sectional area; IOD: inner-to-outer wall distance; SC: Schlemm's canal; SD: standard deviation; TM: trabecular meshwork
* indicates P = 0.01; † indicates P = 0.04; # indicates P = 0.05

3.3. SC parameters

Overall total SC-CSA increased following iStent insertion (P=0.05). When examining each quadrant individually, an increasing, but not statistically significant, trend in SC-CSA was observed in both the nasal and temporal quadrants (P = 0.10 and P = 0.45). There were no significant changes in SC length overall (P = 0.18). Furthermore, no significant changes were observed in either the nasal or temporal quadrant individually (P = 0.22 and P = 0.64, respectively) (Table 2).

An overall trend of increasing SC-IOD was observed after iStent insertion. Total SC-IOD and nasal quadrant SC-IOD increased significantly (2.35 micrometers; P=0.01 and 2.96 micrometers; P = 0.04). There were no significant changes in temporal quadrant SC-IOD following iStent insertion (1.45 micrometers; P = 0.24) (Table 2).

4. Discussion

We found that insertion of the iStent micro-bypass device significantly increased the width of SC, as measured by the SC-IOD parameter, in the nasal quadrant adjacent to the point of insertion. Additionally, a non-significant trend of increasing SC-CSA was observed within the nasal quadrant. There were no significant changes to SC parameters in the temporal quadrant observed. This may suggest that introduction of a local region of reduced outflow resistance within the nasal quadrant does not alter outflow structures elsewhere in SC.

Bahler *et al.* have shown that insertion of a single iStent device increases ocular outflow facility of normal enucleated eyes by 84%.[26] Similarly, Fernandez-Barrientos *et al.* demonstrated an increase in outflow facility by 157% in living human eyes following insertion of 2 iStent devices.[27] Yuan and colleagues have mathematically modeled outflow facility following iStent insertion, and predicted that TM bypass may result in increased SC pressure, reflecting that of the IOP. This increased pressure may then cause dilation of SC and higher flow rates within the SC and downstream collector channels, resulting in the observed increased outflow facility.[28] The present study suggests that bypass of the TM may in fact dilate the SC locally, perhaps due to increased pressures from aqueous humor inflow. As previously demonstrated, the SC is a dynamic structure, collapsing in response to glaucoma and acutely elevated IOP.[10,19,22,23] As these conditions promote collapse of SC structures, increasing inflow and pressure within the SC may promote local dilatory effects.

The dilatory effect of iStent implantation has been noted in a published case study. Gillmann *et al.* found a SC diameter of 390 micrometers after implantation of two devices in a 74-year-old female patient.[29] The authors compared their finding to the observed average SC diameter of 122 µm, suggesting a device effect and not an idiopathic finding. While the effect of implantation appears to be large, note that the SC diameter was compared to a normative average SC diameter of 122 micrometers, and not a pre- *vs* post-surgery comparison. Also, the authors used two devices, as compared to the single device implantation employed in the present study. Nevertheless, the observation of larger-than-expected SC diameter supports the hypothesis that iStent implantation has a favorable impact on outflow structure morphology.

We consider an alteration of outflow morphology to be favorable if it is associated with increased aqueous humor outflow facility. In a recent study of distal outflow structure filling before and after iStent implantation, Huang *et al.* observed subjective improvements in the filling of outflow structures by angiographic methods.[30] Using indocyanine green (ICG) to establish baseline flow patterns, and fluorescein to describe post-implant filling patterns, the authors found improved filling patterns regions characterized by poor filling at baseline, as well as those characterized by faster baseline filling. This suggested that iStent

implantation had a favorable effect on outflow whether implanted in regions of low or high baseline.[30] Taking these findings and those of the present study together, there appears to be structure/function agreement between alterations in outflow morphology within SC, and outflow as represented by angiography immediately after device implantation. However, these findings are unable to predict if this synergistic structure/function relationship persists long-term.

An interesting finding from this study was the trend of increasing temporal SC parameters following iStent insertion. As previously mentioned, we hypothesized that iStent may result in SC dilation in regions adjacent to the nasal insertion site. As aqueous humor outflow facility increases in this region, we predicted a collapse in outflow morphology in more distant regions. This prediction was based on the assumption that aqueous humor would drain predominantly from the dilated regions closest to the iStent device and with the highest outflow facility. As a result, we predicted that distant SC regions may experience lower pressures and ultimately collapse. This, however, was not observed. It is possible that SC patency is either maintained or increased circumferentially across the entirety of the ocular limbus. Previous work has described the presence of myofibroblast-like cells and direct insertions of the ciliary muscle within the TM.[31,32] Both relaxation of these myofibroblast-like cells and contraction of the ciliary muscle can reduce outflow resistance, and it may be possible that these structures play a role in maintaining the patency of the distal outflow structures relative to the point of iStent insertion.

This study had several limitations. First, this study included a small patient sample from a single institution, which may affect the generalizability of its findings. Additionally, our protocol did not dictate a specific time window for which patients were required to obtain postoperative imaging. In order to maximize recruitment, all available post-implant visits were used. Despite these limitations, a statistically significant difference in SC-IOD was detected in the nasal quadrant, suggesting that iStent opens the SC adjacent to its point of insertion. Another potential limitation of this study is the ability of current SD-OCT to discriminate the smallest structures of SC with adequate resolution. Attempts to improve this discriminative ability and resolution of commercially available SD-OCT were made through the technique of averaging, as has been demonstrated in previous studies.[19,24] Despite potential error in estimation of true SC parameters such as SC-CSA, SC length, and ultimately, the calculation of SC-IOD, the limited resolution of commercial SD-OCT capabilities were able to detect a significant increase in SC-IOD in the nasal quadrant following iStent insertion. This study serves as a starting point for understanding the important morphological effects surgically implanted devices such as iStent have on the living human eye. Lastly, our study was limited by the natural variability of SC across its circumferential course around the eye. Because the SC is not uniform circumferentially around the eye, changes in SC parameters, both nasally and temporally, may vary

individually with the location of iStent placement. Furthermore, measurement of SC parameters at one location may considerably differ from other measurements taken nearby. To minimize this potential error, we employed an average of consecutive, equally spaced, measurements across a 1 mm sample in order to obtain each SC parameter, an important technique we have previously demonstrated.[19,33] Thus, each measurement was not a random sample of each parameter, but an average of these parameters across a 1 mm section. Ideally, in order to fully ascertain the mean response of SC parameters following iStent, a 360° scan of the entire limbus and SC would need to be developed.

5. Conclusion

iStent implantation significantly increases SC-IOD in the nasal quadrant, while leaving structures in the temporal quadrant unaffected. These results could influence the surgical decision of implantation in more than one quadrant, as previously suggested. Indeed, multiple devices may be able to increase dramatically the IOD in other parts of the TM circumference and thus facilitate aqueous humor outflow. Looking at the collector channel location and adjusting implantation to the individual SC's and distal outflow structure morphology might be a valuable approach for future studies and clinical outcomes.

Acknowledgements

This abstract was featured as a poster presentation at The Association for Research in Vision and Ophthalmology 2015 Annual Meeting on May 5, 2015.

Dr. Schuman wishes to disclose that he received royalties for intellectual property licensed by the Massachusetts Institute of Technology and Massachusetts Eye and Ear Infirmary to Zeiss, Inc.

The contents of this publication are the sole responsibility of the author(s) and do not necessarily reflect the views, opinions, or policies of Uniformed Services University of the Health Sciences (USUHS), the US Food and Drug Administration, the Department of Defense (DoD), the Departments of the Army, Navy, or Air Force. Mention of trade names, commercial products, or organizations does not imply endorsement by the US Government.

This work was supported in part by National Institutes of Health (Bethesda, MD, USA) contracts R01-EY13178, and P30-EY08098, the Eye and Ear Foundation (Pittsburgh, PA, USA), and unrestricted grants from Research to Prevent Blindness (New York, NY, USA).

References

1. Quigley HA, Broman AT. The number of people with glaucoma worldwide in 2010 and 2020. Br J Ophthalmol. 2006;90(3):262-267.
2. Sommer A, Tielsch JM, Katz J, et al. Racial differences in the cause-specific prevalence of blindness in east Baltimore. N Engl J Med. 1991;325(20):1412-1417.
3. Sommer A, Tielsch JM, Katz J, et al. Relationship between intraocular pressure and primary open angle glaucoma among white and black Americans. The Baltimore Eye Survey. Arch Ophthalmol. 1991;109(8):1090-1095.
4. Mitchell P, Lee AJ, Rochtchina E, Wang JJ. Open-angle glaucoma and systemic hypertension: the blue mountains eye study. J Glaucoma. 2004;13(4):319-326.
5. Leske MC, Wu SY, Hennis A, Honkanen R, Nemesure B. Risk factors for incident open-angle glaucoma: the Barbados Eye Studies. Ophthalmology. 2008;115(1):85-93.
6. Leske MC, Connell AM, Wu SY, Hyman L, Schachat AP. Distribution of intraocular pressure. The Barbados Eye Study. Arch Ophthalmol. 1997;115(8):1051-1057.
7. Mitchell P, Smith W, Attebo K, Healey PR. Prevalence of open-angle glaucoma in Australia. The Blue Mountains Eye Study. Ophthalmology. 1996;103(10):1661-1669.
8. Gabelt BK, P. Adler's Physiology of the Eye. St. Louis, MO: Mosby; 2003.
9. Tamm ER. The trabecular meshwork outflow pathways: structural and functional aspects. Exp Eye Res. 2009;88(4):648-655.
10. Hong J, Xu J, Wei A, et al. Spectral-domain optical coherence tomographic assessment of Schlemm's canal in Chinese subjects with primary open-angle glaucoma. Ophthalmology. 2013;120(4):709-715.
11. Grant WM. Experimental aqueous perfusion in enucleated human eyes. Arch Ophthalmol. 1963;69:783-801.
12. Jocson VL, Sears ML. Experimental aqueous perfusion in enucleated human eyes. Results after obstruction of Schlemm's canal. Arch Ophthalmol. 1971;86(1):65-71.
13. Ahmed, II, Katz LJ, Chang DF, et al. Prospective evaluation of microinvasive glaucoma surgery with trabecular microbypass stents and prostaglandin in open-angle glaucoma. J Cataract Refract Surg. 2014;40(8):1295-1300.
14. Arriola-Villalobos P, Martinez-de-la-Casa JM, Diaz-Valle D, Fernandez-Perez C, Garcia-Sanchez J, Garcia-Feijoo J. Combined iStent trabecular micro-bypass stent implantation and phacoemulsification for coexistent open-angle glaucoma and cataract: a long-term study. Br J Ophthalmol. 2012;96(5):645-649.
15. Fea AM. Phacoemulsification versus phacoemulsification with micro-bypass stent implantation in primary open-angle glaucoma: randomized double-masked clinical trial. J Cataract Refract Surg. 2010;36(3):407-412.
16. Fea AM, Belda JI, Rekas M, et al. Prospective unmasked randomized evaluation of the iStent inject ((R)) versus two ocular hypotensive agents in patients with primary open-angle glaucoma. Clin Ophthalmol. 2014;8:875-882.
17. Samuelson TW, Katz LJ, Wells JM, Duh YJ, Giamporcaro JE. Randomized evaluation of the trabecular micro-bypass stent with phacoemulsification in patients with glaucoma and cataract. Ophthalmology. 2011;118(3):459-467.

18. Spiegel D, Wetzel W, Neuhann T, et al. Coexistent primary open-angle glaucoma and cataract: interim analysis of a trabecular micro-bypass stent and concurrent cataract surgery. Eur J Ophthalmol. 2009;19(3):393-399.
19. Kagemann L, Wang B, Wollstein G, et al. IOP elevation reduces Schlemm's canal cross-sectional area. Invest Ophthalmol Vis Sci. 2014;55(3):1805-1809.
20. Kagemann L, Wollstein G, Ishikawa H, et al. Identification and assessment of Schlemm's canal by spectral-domain optical coherence tomography. Invest Ophthalmol Vis Sci. 2010;51(8):4054-4059.
21. Kagemann L, Wollstein G, Ishikawa H, et al. 3D visualization of aqueous humor outflow structures in-situ in humans. Exp Eye Res. 2011;93(3):308-315.
22. Hong J, Yang Y, Wei A, et al. Schlemm's canal expands after trabeculectomy in patients with primary angle-closure glaucoma. Invest Ophthalmol Vis Sci. 2014;55(9):5637-5642.
23. Wang F, Shi G, Li X, et al. Comparison of Schlemm's canal's biological parameters in primary open-angle glaucoma and normal human eyes with swept source optical. J Biomed Opt. 2012;17(11):116008.
24. Hammer D, Ferguson RD, Iftimia N, et al. Advanced scanning methods with tracking optical coherence tomography. Opt Express. 2005;13(20):7937-7947.
25. Dietlein TS, Jacobi PC, Luke C, Krieglstein GK. Morphological variability of the trabecular meshwork in glaucoma patients: implications for non-perforating glaucoma surgery. Br J Ophthalmol. 2000;84(12):1354-1359.
26. Bahler CK, Smedley GT, Zhou J, Johnson DH. Trabecular bypass stents decrease intraocular pressure in cultured human anterior segments. Am J Ophthalmol. 2004;138(6):988-994.
27. Fernandez-Barrientos Y, Garcia-Feijoo J, Martinez-de-la-Casa JM, Pablo LE, Fernandez-Perez C, Garcia Sanchez J. Fluorophotometric study of the effect of the glaukos trabecular microbypass stent on aqueous humor dynamics. Invest Ophthalmol Vis Sci. 2010;51(7):3327-3332.
28. Yuan F, Schieber AT, Camras LJ, Harasymowycz PJ, Herndon LW, Allingham RR. Mathematical Modeling of Outflow Facility Increase With Trabecular Meshwork Bypass and Schlemm Canal Dilation. J Glaucoma. 2015.
29. Gillmann K, Bravetti GE, Mansouri K, Mermoud A. Anterior Segment Optical Coherence Tomography Signs of Local Dilatation Effect of a Micro-Stent on Schlemm's Canal. Nepal J Ophthalmol. 2018;10(20):184-187.
30. Huang AS, Penteado RC, Papoyan V, Voskanyan L, Weinreb RN. Aqueous Angiographic Outflow Improvement after Trabecular Microbypass in Glaucoma Patients. Ophthalmol Glaucoma. 2019;2(1):11-21
31. Tamm ER, Braunger BM, Fuchshofer R. Intraocular Pressure and the Mechanisms Involved in Resistance of the Aqueous Humor Flow in the Trabecular Meshwork Outflow Pathways. Prog Mol Biol Transl Sci. 2015;134:301-314.
32. de Kater AW, Spurr-Michaud SJ, Gipson IK. Localization of smooth muscle myosin-containing cells in the aqueous outflow pathway. Invest Ophthalmol Vis Sci. 1990;31(2):347-353.
33. Kagemann L, Nevins JE, Jan NJ, et al. Characterisation of Schlemm's canal cross-sectional area. Br J Ophthalmol. 2014;98 Suppl 2:ii10-14.

© Journal for Modeling in Ophthalmology 2020; 4:55-66
Original article

Effects of the hand-grip test on retinal vascular and structural parameters measured by optical coherence tomography in healthy subjects

Carlo Alberto Cutolo[1,2], Lorenzo Ferro Desideri[1,2], Chiara Bonzano[1,2], Felice Cardillo Piccolino[3], Alice Chandra Verticchio Vercellin[4,5,6], Carlo Enrico Traverso[1,2], Massimo Nicolò[1,2,3]

[1]Clinica Oculistica, DiNOGMI, University of Genoa, Italy; [2]Ospedale Policlinico San Martino, Genoa, Italy; [3]Fondazione per la Macula Onlus, Clinica Oculistica, DiNOGMI, University of Genoa, Italy; [4]Department of Ophthalmology, Icahn School of Medicine at Mount Sinai Hospital, New York, NY, USA; [5]University of Pavia, Pavia, Italy; [6]IRCCS – Fondazione Bietti, Rome, Italy

Abstract

Purpose: To examine the relationship between the cardiovascular status and variations in optical coherence tomography (OCT)-derived parameters of the peripapillary and macular tissues, and macular vascular flow area measured by optical coherence tomography angiography (OCTA) in healthy subjects.
Design: Prospective, open-label, non-randomized clinical study.
Methods: Twenty one eyes of 21 healthy subjects were analyzed using a swept-source device, including OCT and OCTA acquisitions. Cardiovascular changes were investigated by performing a practical hand-grip test (HGT). Blood pressure, heart rate, OCT and OCTA structural and vascular changes were measured and analyzed before and after the HGT-induced exercise.
Results: The mean patient age was 34.0 (± 15.2) years. While both diastolic and systolic blood pressures increased significantly after exercise ($p < 0.001$ and $p = 0.003$, respectively), the heart rate did not show a significant increment

Correspondence: Carlo Alberto Cutolo, Clinica Oculistica, Viale Benedetto XV 5, 16132, Genova (GE), Italy.
E-mail: cacutolo@gmail.com

($p = 0.182$). OCT structural parameters of the optic nerve did not change significantly. Instead, a significant redistribution of choroidal thickness (CT) was observed in the macular region, with a significant reduction (-6.5%, $p = 0.001$) in the outer-nasal macular sector after exercise. OCTA acquisitions did not show changes in the vascular density of both the superficial retinal layer and deep retinal layer.
Conclusions: We demonstrated that HGT-induced exercise can moderately elevate blood pressure without detectable effects on OCTA-derived parameters in healthy young subjects. Moreover, it produced a significant redistribution of CT. Further studies are needed to better explain the possible role of HGT in the characterization of the pathophysiology of ocular diseases associated with abnormalities of the vascular function such as glaucoma, age-related macular degeneration, and diabetic retinopathy.

Keywords: choroidal thickness, exercise, hand-grip test, ocular blood flow, optical coherence tomography, retinal vessels

1. Introduction

The retina represents one of the most metabolically active tissues in the body, since it receives a double blood supply deriving from both the retinal and choroidal circulations.[1] The growing interest in studying the retinal and choroidal structure and blood flow relies on the possibility of further understanding the pathophysiology of potentially blinding disorders such as age-related macular degeneration, glaucoma, and diabetic retinopathy. Nowadays, optical coherence tomography (OCT) represents a widely used non-invasive imaging technique to assess changes in the structure of the different anatomical regions of the retina caused by pathologic processes. Several imaging methods are also available to assess the retinal and choroidal blood flow; however, to date, none has been recognized as gold standard.[2-4] Laser Doppler flowmetry (LDF) is a non-invasive technique that measures the Doppler shift caused by the movement of erythrocytes.[5] Several studies analyzed the different factors influencing choroidal blood flow measured by LDF during isometric exercise, showing the complex regulatory mechanisms associated with variations in mean arterial pressure (MAP), intraocular pressure (IOP), and ocular perfusion pressure (OPP).[6,7] Furthermore, laser speckle flowgraphy is another novel non-invasive technique based on the interference phenomenon, and it has shown reproducible data and a good reliability profile with LDF in the study of choroidal blood flow.[8] Doppler optical coherence tomography (Doppler-OCT) is another diagnostic tool studied for the retinal and choroidal analysis; however, further *in vivo* studies are needed in order to better clarify its clinical reliability.[9]

Optical coherence tomography angiography (OCTA) is a novel, non-dye-based imaging technique for visualization and assessment of the retinal vasculature.[10-12] Alnawaiseh *et al.* were the first to use OCTA to evaluate the variations induced by exercise in the retinal vascularization of healthy subjects. The authors found a significant change in flow densities associated with systemic cardiovascular modifications (blood pressure [BP]).[13] Understanding the relationship between the patient's cardiovascular status and OCT/OCTA measurements is meaningful to the clinician because altered cardiovascular status may affect the measurements of the exam, potentially leading to misinterpretation of the results. Moreover, a hand-grip exercise that dynamically changes the results of OCT/OCTA could help to elucidate the pathophysiology of ocular diseases as recently showed for central serous chorioretinopathy, where an impairment of retinal vessel autoregulation was reported.[14]

In this study, we investigated the changes induced by a practical hand-grip test (HGT) on the OCT-derived parameters of the peripapillary and macular tissues and on the macular vasculature measured by OCTA in healthy subjects.

2. Methods

2.1. Baseline visit

This study enrolled healthy volunteers of both sexes all with ages above 18 years and without any systemic or ocular disease. The research was conducted at Clinica Oculistica, Ospedale Policlinico San Martino - IRCCS, Italy from January to March 2018. All procedures followed the tenets of the Declaration of Helsinki and informed consent was obtained from all the subjects. All the subjects completed a full ophthalmological examination, including best-corrected visual acuity (BCVA), slit-lamp examination, IOP measurement with Goldmann applanation tonometry. Optical biometry by Lenstar LS 900 (Haag-Streit AG, Köniz, Switzerland) was used to measure the axial length and central corneal thickness. Pupil dilation was obtained with tropicamide 1% eye drop (Visumidriatic, Visufarma Spa, Italy) and fundoscopy was performed using a 90-diopter hand-held lens. Eyes with a history of previous intraocular surgery as well as subjects affected by any systemic disease, diabetes, hypertension and other ocular or systemic disorders known to impair the diagnostic procedures were excluded. Eyes were also excluded if they had BCVA worse than 0.10 LogMAR and a refractive error outside the range −6.00 to +3.00 D. Each subject was asked to refrain from smoking and caffeine intake for at least 60 minutes before any examination to minimize the influence of these substances on the cardiovascular parameters.[15] Blood pressure (BP) and heart rate (HR) were measured using an automated sphygmomanometer (HEM-907, Omron Europe B.V, The Netherlands) with subjects in a seated position, after at least a five-minute resting period. The resting BP value was considered as the average of two readings taken at least five

minutes apart in the same arm. The arm selected for the measurements was the non-dominant and the sphygmomanometer wrist was set at the level of the heart. One qualified eye was randomly selected as the study eye, and underwent OCT and OCTA assessment (details below).

2.2. OCT

A single, wide-field, swept-source OCT scan (DRI OCT-1 Atlantis, Topcon, Inc., Tokyo, Japan) was completed. The wide-field SS-OCT scan consists of a 9 x 12 mm rectangle that covered both the macular and disc regions and is formed by 256 b-scans, each with 512 a-scans. Only scans with an image quality index above 40 were considered for analysis. All images were reviewed for segmentation errors. Circumpapillary retinal nerve fiber layer (cpRNFL) and choroid thickness were extracted using the OCT instrument's software in the following quadrants and sectors: temporal, temporal-superior, temporal-inferior, nasal, nasal-superior, and nasal-inferior. Retinal and choroidal thicknesses were analyzed accordingly with the nine macular sectors defined by the Early Treatment Diabetic Retinopathy Study (ETDRS) (center, inner-temporal, inner-superior, inner-nasal, inner-inferior, outer-temporal, outer-superior, outer-nasal, and outer-inferior).

2.3. OCTA

OCTA scans were acquired immediately after structural OCT, with the same instrument. The scans were taken from a 4.5 x 4.5 cube, with each cube consisting of 320 clusters of four repeated b-scans centered on the fovea. The automated layer segmentation performed by the OCT instrument software (IMAGEnet 6, Topcon) displayed *en-face* images of the microvasculature of the superficial retinal layer (SRL) and deep retinal layer (DRL) in the central region and four quadrants (superior, inferior, nasal, and temporal). The instrument's segmentation software defines the *en-face* slab for the SRL from 2.6 µm beneath the internal limiting membrane to 15.6 µm beneath the interface of the inner plexiform layer and inner nuclear layer (IPL/INL). The DRL slab was considered from 15.6 µm beneath the IPL/INL to 70.2 µm beneath the IPL/INL. All images were reviewed for segmentation errors for the SRL and DRL. Vascular densities of the SRL (vd-SRL) and DRL (vd-DRL) were calculated using the instrument's software.

2.4. Hand-grip exercise and OCT measurements

The experimental protocol was adapted from the work of Cardillo Piccolino *et al.*[14] After cardiovascular and OCT measurements at rest, the HGT was then performed on the dominant side by using a Jamar hand dynamometer (Lafayette Instruments, Lafayette, IN, USA). The subject was asked to squeeze the handle three times with their maximum hand strength, and 30% of the mean of the measurements was recorded. Then, the subject was asked to perform the hand-grip exercise maintaining 30% of their maximum hand strength for 3 to 5 minutes. OCT and OCTA scans were

performed in the same eye of the resting measurements after two minutes from the start of the isometric effort. BP and HR were also measured.

2.5. Statistical analysis

In descriptive statistics, variables were summarized as means and standard deviation. Comparisons between resting and exercise values for each parameter were performed with the Wilcoxon signed-rank test. *P* values less than 0.05 are considered statistically significant. Because multiple tests were performed of the same dataset, the Benjamini-Hochberg procedure was used to correct for the false discovery rate to avoid that *p* values less than 0.05 were purely by chance. Computerized statistical analyses were performed with STATA software (version 15.1, STATACorp, TX, USA).

3. Results

We analyzed the data of 21 eyes of 21 subjects. All the OCT and OCTA scans had an adequate quality (image quality index > 40), and no segmentation errors were detected. Table 1 summarizes the demographics and ocular characteristics of the enrolled healthy subjects. The mean (± standard deviation) age was 34.0 (± 15.2) years and 66.7% were women. The dominant hand, which performed the HGT, was the right for 18 (85.7%) subjects. Hence, only 3 (14.3%) subjects had BP assessment in the right arm. Table 2 shows the changes in the cardiovascular parameters before and during HGT. Both diastolic and systolic BP significantly increased, whereas the

Table 1. Demographics and ocular characteristics of the study subjects

	N = 21 eyes
Age, years	34.0 (±15.2)
Gender, female	14 (66.7%)
Eye, right	12 (57.1%)
IOP, mmHg	13.6 (± 2.5)
CCT, µm	545 (± 30)
Axial length, mm	23.6 (± 0.8)
Sphere equivalent, D	-0.85 (± 2.13)
Visual acuity, LogMAR	0.00
Hand-grip maximal voluntary contraction, kg-force	33.7 (± 8.6)
Dominant hand, right	18 (85.7%)

CCT: central corneal thickness; IOP: intraocular pressure; N: number of eyes
Data are number (%) or mean (± SD).

Table 2. Cardiovascular changes of the study subjects

	Baseline	Exercise	Difference	p-value
Diastolic BP, mmHg	76.3 (± 8.6)	88.9 (± 11.7)	+ 12.6 (± 10.5)	< 0.001
Systolic BP, mmHg	123.2 (± 15.3)	135.2 (± 19.0)	+ 12.0 (± 16.3)	0.003
Hearth rate, bpm	84.3 (± 19.2)	89.1 (± 20.8)	+ 4.8 (± 13.6)	0.182

BP: blood pressure; bpm: beats per minute

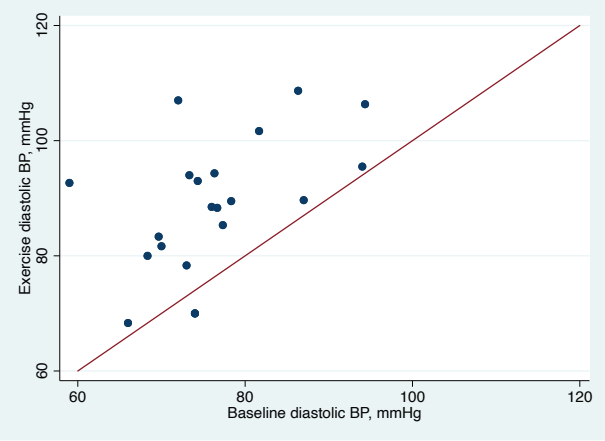

Fig. 1. The effect of exercise on diastolic blood pressure.

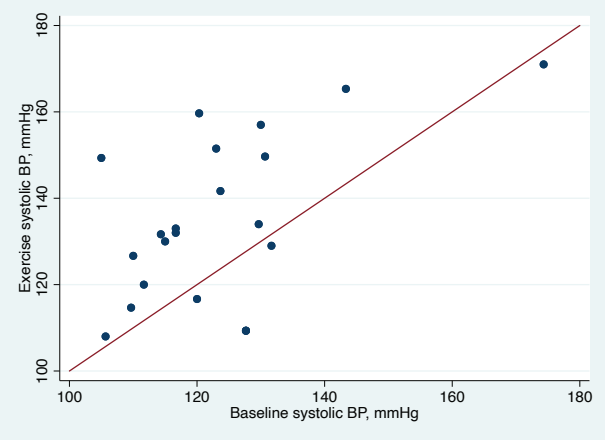

Fig. 2. The effect of exercise on systolic blood pressure.

HR increment was not statistically significant. Figures 1 and 2 show the effect of exercise on diastolic and systolic BP. The majority of subjects were located above the 'no effect' line. One and four subjects were located below the 'no effect' line for the diastolic and systolic parameter, respectively. Mean percentage changes during exercise were +16.5% and +9.7% for diastolic and systolic BP, respectively. Table 3 shows the structural changes in the cpRNFL and choroidal thickness (CT) assessed via OCT. After correction for the false discovery rate, none of the structural OCT parameters of the optic nerve changed significantly. When analyzing the structural changes of the retinal and choroidal tissues in the macular region (Table 4), we observed a statistically significant redistribution of CT. Namely, the outer-nasal sector showed a mean reduction of -6.5% (p = 0.001) during the isometric exercise. As shown in Table 5, no significant vessel density changes in the SRL and DRL were measured by OCTA.

Table 3. Circumpapillary retinal nerve fiber layer and choroidal thickness assessed by optical coherence tomography

	Baseline	**Exercise**	**Difference**	***p*-value**
cpRNFL, temporal, µm	132 (± 19)	134 (± 21)	+ 2 (± 25)	0.766
cpRNFL, temporal-superior, µm	122 (± 27)	116 (± 26)	- 7 (± 14)	0.048
cpRNFL, nasal-superior, µm	89 (± 16)	84 (± 14)	- 5 (± 16)	0.1499
cpRNFL, nasal, µm	134 (± 28)	127 (± 25)	- 7 (± 19)	0.1243
cpRNFL, nasal-inferior, µm	147 (± 19)	147 (± 32)	0 (± 27)	0.9609
cpRNFL, temporal-inferior, µm	149 (± 10)	148 (± 10)	- 1 (± 5)	0.1647
cpChoroid, temporal, µm	144 (± 69)	149 (± 75)	+ 5 (± 31)	0.4538
cpChoroid, temporal-superior, µm	138 (± 69)	143 (± 71)	+ 4 (± 19)	0.3179
cpChoroid, nasal-superior, µm	129 (± 57)	133 (± 55)	+ 4 (± 19)	0.3321
cpChoroid, nasal, µm	109 (± 60)	117 (± 66)	+ 8 (± 24)	0.1436
cpChoroid, nasal-inferior, µm	108 (± 64)	115 (± 74)	+ 7 (± 42)	0.4803
cpChoroid, temporal-inferior, µm	47 (± 6)	46 (± 4)	0 (± 4)	0.6498

cpRNFL: circumpapillary retinal nerve fiber layer thickness; cpChoroid: circumpapillary choroid
Data are mean (SD).

Table 4. Retinal and choroidal thicknesses in the macular region assessed by OCT

	Baseline	**Exercise**	**Difference**	***p*-value**
Retina, center, µm	305 (± 15)	305 (± 5)	+ 1 (± 3)	0.1128
Retina, inner-temporal, µm	308 (± 38)	316 (± 12)	+ 8 (± 38)	0.3153
Retina, inner-superior, µm	316 (± 14)	317 (± 11)	+ 2 (± 9)	0.3473
Retina, inner-nasal, v	305 (± 41)	314 (± 13)	+ 9 (± 42)	0.3378
Retina, inner-inferior, µm	264 (± 13)	263 (± 11)	- 1 (± 7)	0.7182
Retina, outer-temporal, µm	268 (± 26)	274 (± 8)	+ 6 (± 25)	0.2788
Retina, outer-superior, µm	292 (± 10)	290 (± 10)	- 2 (± 8)	0.3756
Retina, outer-nasal, µm	262 (± 27)	269 (± 10)	+ 8 (± 26)	0.1849
Retina, outer-inferior, µm	279 (± 15)	280 (± 9)	+ 1 (± 14)	0.7045
Choroid, center, µm	280 (± 66)	278 (± 65)	- 2 (± 7)	0.2259
Choroid, inner-temporal, µm	265 (± 67)	264 (± 70)	- 1 (± 14)	0.7124
Choroid, inner-superior, µm	244 (± 71)	243 (± 71)	+ 1 (± 9)	0.5662
Choroid, inner-nasal, µm	277 (± 66)	278 (± 65)	+ 1 (± 11)	0.6760
Choroid, inner-inferior, µm	265 (± 52)	264 (± 52)	- 2 (± 7)	0.2812
Choroid, outer-temporal, µm	254 (± 69)	253 (± 68)	- 2 (± 9)	0.4247
Choroid, outer-superior, µm	188 (± 74)	189 (± 73)	+ 1 (± 5)	0.4138
Choroid, outer-nasal, µm	263 (± 65)	246 (±58)	- 16 (± 20)	0.0014*
Choroid, outer-inferior, µm	106 (± 9)	103 (± 11)	- 3 (± 8)	0.1277

*P-value remained statistically significant after correction for the false discovery rate. Data are mean (SD).

Table 5. Macular vessel density assessed by OCTA

	Baseline	Exercise	Difference	p-value
Vd-SRL, central	47.3 (± 4.1)	47.2 (± 5.3)	- 0.1 (± 6.5)	0.9428
Vd-SRL, superior	16.5 (± 3.5)	16.9 (± 4.3)	+ 0.4 (± 2.3)	0.4324
Vd-SRL, inferior	42.9 (± 3.3)	45.1(± 2.5)	+ 2.3 (± 2.7)	0.0127
Vd-SRL, nasal	46.5 (± 2.7)	46.8 (± 2.6)	+ 0.3 (± 2.6)	0.6206
Vd-SRL, temporal	40.0 (± 2.6)	40.5 (± 2.1)	+ 0.5 (± 2.5)	0.3847
Vd-DRL, central	52.4 (± 8.0)	51.6 (± 2.4)	- 0.8 (± 8.2)	0.6636
Vd-DRL, superior	15.3 (± 4.4)	16.2 (± 4.3)	+ 0.9 (± 3.7)	0.2656
Vd-DRL, inferior	50.4 (± 4.9)	49.7 (± 3.6)	- 0.7 (± 3.5)	0.5506
Vd-DRL, nasal	49.0 (± 2.6)	49.0 (± 2.6)	0.0 (± 3.3)	0.9847
Vd-DRL, temporal	43.6 (± 2.0)	43.1 (± 1.9)	- 0.4 (± 2.5)	0.4429

vd-DRL: vessel density of the deep retinal layer, %; vd-SRL: vessel density of the superficial retinal layer, % Data are mean (SD).

4. Discussion

In the present study, we tested the hypothesis that perturbation of the cardiovascular status caused by an isometric exercise significantly affects the structural and vascular OCT measurements. We found that only slight changes in the CT in the macular region occurred during the exercise.

Recently, Cardillo Piccolino *et al.* applied a similar methodology to demonstrate an increase of retinal blood flow in central serous chorioretinopathy patients. They also found no significant changes in the control group of age-matched healthy subjects using 85-kHz spectral-domain OCT with a wavelength of 870 nm.[14] Conversely to the Cardillo Piccolino's study, we used 100-kHz swept-source OCT with a wavelength of 1050 nm, allowing better penetration of light into the choroidal tissue and thus, better delineation of the sclero-choroidal junction and reliable CT measurements.[16] Swept-source OCT allows automatic analysis of CT in the peripapillary and macular area, which seems to be related to choroidal blood flow.[17] After the isometric exercise, the redistribution of choroidal blood flow appears to cause the reduction of the CT detected by swept-source OCT.

In healthy eyes, retinal blood flow is highly autoregulated by an intrinsic mechanism that changes the myogenic tone accordingly to the perfusion pressure, whereas choroidal circulation is mainly controlled by the extrinsic autonomic innervation.[18-20] Namely, the reduction in choroidal blood flow is driven by the sympathetic nervous system, while the increases are driven by the parasympathetic nervous system.[21] The HGT can cause a reduction of the parasympathetic nervous

system, followed by an increase of sympathetic stimulation.[22] As shown in Figures 1 and 2, the HTG elicited an increase in diastolic and systolic BP in the vast majority of subjects. However, even for subjects whose BP does not increase, the HTG can cause changes in the autonomic nervous system which can affect the ocular blood flow. Changes in the autonomic innervation of the choroid elicited by the HGT may explain the slight but significant reduction in CT observed in the present study. Using LDF, Bata *et al.* also found a reduction of choroidal blood flow during HGT in a limited number of individuals of a cohort of healthy subjects and glaucoma patients.[23]

In a cohort of 40 healthy subjects, Kim *et al.* demonstrated a reduction of the vd-DRL after 20 minutes of maximal physical exercise consisting of riding a training bike reaching 85% of maximum theoretical HR.[24] The strength of this work is that Kim *et al.* obtained changes detectable by OCTA. However, this exercise could be impractical in the clinical setting compared to the HGT, which is relatively easy to perform and has been validated in many clinical studies.[14,23,25–27] Alnawaiseh *et al.* also showed a reduction of the peripapillary and parafoveal flow density immediately after a specific training program that included sit-ups, push-ups, squats, lunges, and rope skipping.[13] Both the intensive program and the training bike exercise reported in the previously cited studies have caused a greater elevation of BP compared to our study (after exercise systolic pressure, mmHg: 141.8 ± 10.1[13]; 167.8 ± 13.8[24] *vs* 135.2 ± 19.0, respectively).

This study is not without limitations. One limitation was the lack of IOP measurement during the exercise since IOP is affected by physical exercise.[28] However, a 3-to-5 minute HGT seems unlikely to cause a considerable change in IOP, and accordingly, in OPP. Additionally, it is important to highlight that the mean age of our study population was 34 years (± 15.2). The results of our study cannot therefore be generalized to older subjects, since changes in the physiologic cardiovascular response to exercise occur with the aging process. The effect of aging on the relationship between exercise, cardiovascular system, and ocular OCT-derived parameters need therefore to be further investigated. Further studies are also needed to investigate the role of gender. Another limitation is the study's small sample size. Finally, studies are needed to compare the effect of exercise on OCT- and OCTA-derived parameters not only in healthy subjects, but also in patients affected by different ocular diseases.

In conclusion, our study showed that the hand-grip exercise is able to moderately elevate BP without detectable effects on OCTA-derived parameters in healthy subjects. We also showed that an easy to perform hand-grip exercise is able to produce small but significant effects on CT. In healthy subjects, a moderate elevation of BP seems unlikely to affect OCTA measurements, whereas it can affect CT. In subsequent studies, the HGT could be used to better define the pathophysiology of ocular diseases considered to be associated with impaired vascular function such as glaucoma, age-related macular degeneration, and diabetic retinopathy.

Acknowledgements

The contribution of Dr. Alice C. Verticchio Vercellin was supported by Fondazione Roma and the Italian Ministry of Health.

References

1. Funk RH. Blood supply of the retina. Ophthalmic Res. 1997;29(5):320–325.
2. Causin P, Guidoboni G, Malgaroli F, Sacco R, Harris A. Blood flow mechanics and oxygen transport and delivery in the retinal microcirculation: multiscale mathematical modeling and numerical simulation. Biomech Model Mechanobiol. 2016;15(3):525–542.
3. Wei X, Balne PK, Meissner KE, Barathi VA, Schmetterer L, Agrawal R. Assessment of flow dynamics in retinal and choroidal microcirculation. Surv Ophthalmol. 2018;63(5):646–664.
4. Verticchio Vercellin AC, Cutolo CA, Dellafiore C, Lava M, Tinelli C, De Silvestri A, et al. Inter-device reproducibility of retrobulbar blood flow velocity measurements in healthy subjects using color Doppler imaging. J Ultrasound. 2016;1–6.
5. Kouadio AA, Jordana F, Koffi NJ, Le Bars P, Soueidan A. The use of laser Doppler flowmetry to evaluate oral soft tissue blood flow in humans: A review. Arch Oral Biol. 2018;86:58–71.
6. Popa-Cherecheanu A, Schmidl D, Werkmeister RM, Chua J, Garhöfer G, Schmetterer L. Regulation of Choroidal Blood Flow During Isometric Exercise at Different Levels of Intraocular Pressure. Invest Ophthalmol Vis Sci. 2019;60(1):176–182.
7. Schmidl D, Schmetterer L, Witkowska KJ, et al. Factors Associated With Choroidal Blood Flow Regulation in Healthy Young Subjects. Invest Ophthalmol Vis Sci. 2016;57(13):5705–5713.
8. Calzetti G, Fondi K, Bata AM, et al. Assessment of choroidal blood flow using laser speckle flowgraphy. Br J Ophthalmol. 2018;102(12):1679–1683.
9. Leitgeb RA, Werkmeister RM, Blatter C, Schmetterer L. Doppler Optical Coherence Tomography. Prog Retin Eye Res. 2014;41:26–43.
10. Kashani AH, Chen C-L, Gahm JK, Zheng F, et al. Optical coherence tomography angiography: A comprehensive review of current methods and clinical applications. Prog Retin Eye Res. 2017;60:66–100.
11. Koustenis A, Harris A, Gross J, Januleviciene I, Shah A, Siesky B. Optical coherence tomography angiography: an overview of the technology and an assessment of applications for clinical research. Br J Ophthalmol. 2017;101(1):16–20.
12. Rodríguez FJ, Staurenghi G, Gale R, Vision Academy Steering Committee. The role of OCT-A in retinal disease management. Graefes Arch Clin Exp Ophthalmol. 2018;256(11):2019–2026.
13. Alnawaiseh M, Lahme L, Treder M, Rosentreter A, Eter N. Short-term effects of exercise on optic nerve and macular perfusion measured by optical coherence tomography angiography. Retina. 2017;37(9):1642.
14. Cardillo Piccolino F, Lupidi M, Cagini C, et al. Retinal Vascular Reactivity in Central Serous Chorioretinopathy. Invest Ophthalmol Vis Sci. 2018;59(11):4425–4433.

15. Kallioinen N, Hill A, Horswill MS, Ward HE, Watson MO. Sources of inaccuracy in the measurement of adult patients' resting blood pressure in clinical settings: a systematic review. J Hypertens. 2017;35(3):421–441.
16. Komma S, Chhablani J, Ali MH, Garudadri CS, Senthil S. Comparison of peripapillary and subfoveal choroidal thickness in normal versus primary open-angle glaucoma (POAG) subjects using spectral domain optical coherence tomography (SD-OCT) and swept source optical coherence tomography (SS-OCT). BMJ Open Ophthalmol. 2019;4(1):e000258.
17. Akahori T, Iwase T, Yamamoto K, Ra E, Terasaki H. Changes in Choroidal Blood Flow and Morphology in Response to Increase in Intraocular Pressure. Invest Ophthalmol Vis Sci. 2017;58(12):5076–5085.
18. Harris A, Arend O, Bohnke K, Kroepfl E, Danis R, Martin B. Retinal blood flow during dynamic exercise. Graefes Arch Clin Exp Ophthalmol. 1996;234(7):440–444.
19. Iester M, Torre PG, Bricola G, Bagnis A, Calabria G. Retinal Blood Flow Autoregulation after Dynamic Exercise in Healthy Young Subjects. Ophthalmologica. 2007;221(3):180–185.
20. Bill A, Sperber GO. Control of retinal and choroidal blood flow. Eye. 1990;4(2):319–325.
21. Kur J, Newman EA, Chan-Ling T. Cellular and physiological mechanisms underlying blood flow regulation in the retina and choroid in health and disease. Prog Retin Eye Res. 2012;31(5):377–406.
22. Martin CE, Shaver JA, Leon DF, Thompson ME, Reddy PS, Leonard JJ. Autonomic Mechanisms in Hemodynamic Responses to Isometric Exercise. J Clin Invest. 1974;54(1):104–115.
23. Bata AM, Fondi K, Witkowska KJ, et al. Optic nerve head blood flow regulation during changes in arterial blood pressure in patients with primary open-angle glaucoma. Acta Ophthalmol (Copenh). 2019;97(1):e36–41.
24. Kim SV, Semoun O, Pedinielli A, Jung C, Miere A, Souied EH. Optical Coherence Tomography Angiography Quantitative Assessment of Exercise-Induced Variations in Retinal Vascular Plexa of Healthy Subjects. Invest Ophthalmol Vis Sci. 2019;60(5):1412–1419.
25. Bond V, Curry BH, Adams RG, Obisesan T, Pemminati S, Gorantla VR, et al. Cardiovascular Responses to an Isometric Handgrip Exercise in Females with Prehypertension. North Am J Med Sci. 2016;8(6):243–249.
26. Walamies M, Turjanmaa V. Assessment of the reproducibility of strength and endurance handgrip parameters using a digital analyser. Eur J Appl Physiol. 1993;67(1):83–86.
27. Khurana RK, Setty A. The value of the isometric hand-grip test-studies in various autonomic disorders. Clin Auton Res. 1996;6(4):211–218.
28. Vera J, Jiménez R, Redondo B, Torrejón A, De Moraes CG, García-Ramos A. Effect of the level of effort during resistance training on intraocular pressure. Eur J Sport Sci. 2019;19(3):394–401.

Journal for Modeling in Ophthalmology

Focus and Scope

While the rapid advance of imaging technologies in ophthalmology is making available a continually increasing number of data, the interpretation of such data is still very challenging and this hinders the advance in the understanding of ocular diseases and their treatment. Interdisciplinary approaches encompassing ophthalmology, physiology, mathematics and engineering have shown great capabilities in data analysis and interpretation for advancing basic and applied clinical sciences.

The Journal for Modeling in Ophthalmology (JMO) was created in 2014 with the aim of providing a forum for interdisciplinary approaches integrating mathematical and computational modeling techniques to address open problems in ophthalmology. JMO welcomes articles that use modeling techniques to investigate questions related to the anatomy, physiology and function of the eye in health and disease.

www.modeling-ophthalmology.com
Published by Kugler Publications
www.kuglerpublications.com